A Radar-Tomographic Bidirectional Method for Quantitative Microwave Breast Imaging

Mutsuki Nakajima and Shouhei Kidera, *Senior Member, IEEE*

***Abstract*— A bidirectional processing method using radar and tomography approaches is proposed to achieve an accurate dielectric profile reconstruction for breast cancer microwave imaging. We introduce a tomography-enhanced radar approach to obtain accurate radar profiles for highly heterogeneous media, where Green's function and clutter components, such as skin reflection, are effectively reconstructed using a contrast source inversion (CSI)-based tomography scheme, that is, "tomography → radar" process. Furthermore, this method introduces a radar-enhanced CSI approach to provide accurate dielectric profiles using an appropriate initial estimate through an accuracy-enhanced radar image. The aforementioned bidirectional processing between radar and tomography consequentially upgrades the reconstruction performance of quantitative imaging (i.e., complex permittivity profile reconstruction) for breast media (radar → tomography process), which would improve the recognition rate for cancerous tissues. The finite-difference time-domain (FDTD)-based numerical test, using realistic breast phantoms, demonstrated that the proposed approach considerably enhances the reconstruction accuracy in permittivity and conductivity.**

***Index Terms*— Complex permittivity reconstruction, contrast source inversion (CSI), inverse scattering (IS) analysis, microwave ultrawide-band (UWB) breast cancer detection, radar imaging.**

I. Introduction

MICROWAVE breast cancer imaging achieves safe, low-cost, compact, pain-free, and frequent (once every few months) monitoring modality, which is hardly accomplished by the existing X-ray mammography technologies. Thus, microwave-based diagnoses strongly help to increase the currently low cancer examination rate (44% in Japan [1]) or increase the recognition rate for early-stage cancer at a size of 10 mm [2], [3], which enhances the survival rate through early treatment. Several studies have reported that a distinct dielectric contrast exists between adipose and malignant tumor tissues [4], [5], [6], [7], which contributes to a strong backscattering and leads to high-contrast images using a focusing algorithm, namely, the radar approach. The radar approach is often called confocal imaging (CI) or beamformer, which coherently synthesizes backscattering signals to enhance spatial resolution [8], [9], [10], [11]. Although the radar approach has advantages such as low complexity, it cannot retrieve the dielectric property of each tissue. In addition, most radar approaches assume homogeneity for breast media. Thus, they considerably suffer from inaccuracy in the case of highly heterogeneous media, namely dense breasts, because densely distributed glandular tissue generates significant reflection, which elicits a strong response in radar images and false-positive diagnoses. A few studies have attempted to modify the propagation model to suit heterogeneous media [12], [13]. Our previous study [13] accurately generated a Green's function for heterogeneous media using the optimizing output obtained by the contrast source inversion (CSI) [14]. This approach also generates a clutter signal using the CSI outputs and can remarkably enhance the signal-to-clutter ratio (SCR). However, certain challenges must be resolved, such as incomplete prior knowledge of dielectric profiles for background media.

Regarding dielectric profile reconstruction, namely quantitative imaging for complex permittivity, there are many studies on inverse scattering (IS) analyses [15], [16], [17], [18], particularly the so-called tomography approach, which directly optimizes the spatial profile of complex permittivity by solving the domain integral equation (DIE). However, the aforementioned inverse problem is usually an ill-posed condition and nonlinear problem, which hinges on an accurate reconstruction with a low-complexity algorithm. To alleviate these IS difficulties, many algorithms can be used, such as linear or nonlinear optimizers [17], [18], [19], [20], [21]. This study focused on the effective IS approach as CSI, which offers a distinct advantage in that it does not require an iterative calculation of the forward solver, such as finite-difference time-domain (FDTD). Notably, CSI does not only optimize an object function (dielectric profile), but also total electric fields within the entire area of the region of interest (ROI), by minimizing the cost functions defined by the state and data equations. Additionally, this approach has been massively introduced in biomedical applications, such as breast cancer detection [22], [23], [24], [25] or brain cerebral hemorrhage [26], [27]. However, CSI still suffers from inaccuracy in the reconstruction of highly heterogeneous (high contrast) media owing to strong nonlinearity or local optimization issues. To address the above difficulty, certain studies integrating the radar approach have been developed [28], [29], [30], by narrowing the ROI corresponding to the high-contrast area, for example, fibroglandular or tumor tissues. Nonetheless, its reconstruction accuracy naturally depends on that of a radar image, which almost always assumes a homogeneous background media. Kurrant and Fear [31] also introduced the time-of-arrival (TOA)-based ROI estimates with average dielectric properties. However, they presume several

Manuscript received 21 February 2023; revised 6 August 2023; accepted 23 August 2023. Date of publication 14 November 2023; date of current version 20 December 2023. This work was supported by the Ministry of Education, Culture, Sports, Science and Technology (MEXT)/Japan Society for the Promotion of Science (JSPS) KAKENHI, Japan, under Grant JP20H02161. *(Corresponding author: Shouhei Kidera.)*

The authors are with the Graduate School of Informatics and Engineering, The University of Electro-Communications, Tokyo 182-8585, Japan (e-mail: kidera@uec.ac.jp).

Color versions of one or more figures in this article are available at https://doi.org/10.1109/TAP.2023.3311101.

Digital Object Identifier 10.1109/TAP.2023.3311101

unpractical assumptions, including one where the TOA values from skin, adipose, or glandular areas are completely separated and that these TOAs are converted to the dielectric constant for each area, using geometrical optics approximation. Note that the study in [32] used prior ultrasound images. However, it required an accurate registration procedure between tomography and ultrasound images.

This article introduces a bidirectional processing algorithm between the radar and tomography methods. The first processing is "tomography → radar," that is, the CSI-based tomography generates an accurate Green's function with a breast model constituting only skin and adipose tissues, which enhances the reconstruction accuracy of the radar image, provided that it only focuses on a high-contrast area, such as fibroglandular or cancerous tissues. This has been partially investigated previously [13]. In the second process, that is, "radar → tomography," the obtained radar image provides an appropriate initial estimate of the CSI reconstruction by converting the strength of the radar image to the complex permittivity. There are some investigations of dependency of initial guess of the IS analysis [18]. Several approaches based on the level set algorithm, which defines the boundary of the low and high contrast area to reduce the number of unknowns, have been also developed [33], [34], [35], using a prior knowledge of dielectric parameter of each tissue. However, there are few studies to provide a radar image-based initial guess for the post-IS approach. Thus, the main contributions of this study are as follows.

1) The CSI-based tomography provides an accurate estimation of Green's function in heterogeneous media and the clutter signal, such as skin surface reflection ("tomography → radar" processing).
2) The radar image offers a promising initial estimate for post-CSI quantitative reconstruction ("radar → tomography"), and the reconstruction accuracy including the high-contrast area (fibroglandular or tumor tissues) is significantly improved.

The FDTD numerical analysis, using a magnetic resonance imaging (MRI)-derived realistic phantom, showed that the proposed scheme could achieve an accurate dielectric profile reconstruction, thereby increasing the cancer recognition rate.

II. Method

A. Observation Model

Fig. 1 shows the 2-D configuration of the observation and target models. The array with numerous transmitters and receivers was located within the breast surrounding area, denoted by Ω_S. The inner area of the breast was defined as the ROI, denoted by Ω_D, and the breast comprised skin, adipose, fibroglandular, and tumor tissues, each of which exhibited dispersive and isotropic dielectric properties. $E^T(\omega; \boldsymbol{r}_T, \boldsymbol{r}_R)$ and $E^I(\omega; \boldsymbol{r}_T, \boldsymbol{r}_R)$ represent the observed total electric fields with and without the breast media, respectively, which are illuminated by the point-source transmitter located at $\boldsymbol{r}_T$ and received at $\boldsymbol{r}_R$. $E^S(\omega; \boldsymbol{r}_T, \boldsymbol{r}_R) \equiv E^T(\omega; \boldsymbol{r}_T, \boldsymbol{r}_R) - E^I(\omega; \boldsymbol{r}_T, \boldsymbol{r}_R)$ is also defined as a scattering electric field.

B. Contrast Source Inversion

To accomplish an accurate quantitative reconstruction of the complex permittivity of the breast, the CSI method is introduced as a promising IS approach. Derived from the

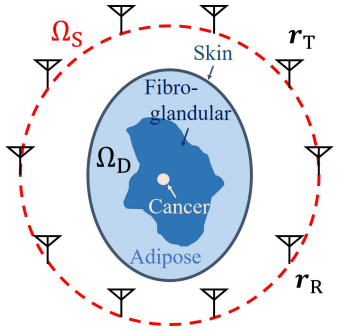

Fig. 1. Observation model. Observation and object areas are defined as Ω_S and Ω_D, respectively.

Helmholtz equations, the scattered electric field $E^S(\omega; \boldsymbol{r}_T, \boldsymbol{r}_R)$ is expressed as

$$E^S(\omega; \boldsymbol{r}_T, \boldsymbol{r}_R) = k_{bg}^2 \int_{\Omega_D} G^{bg}(\omega; \boldsymbol{r}, \boldsymbol{r}_R) w(\omega; \boldsymbol{r}_T, \boldsymbol{r}) d\boldsymbol{r} \quad (1)$$

where k_{bg} and $G^{bg}(\omega; \boldsymbol{r}, \boldsymbol{r}_R)$ are the wavenumber and Green's function of the background media, respectively. $w(\omega; \boldsymbol{r}_T, \boldsymbol{r}) \equiv \chi(\omega; \boldsymbol{r}) E^T(\omega; \boldsymbol{r}_T, \boldsymbol{r})$ is the contrast source, where $\chi(\omega; \boldsymbol{r}) \equiv (\epsilon(\boldsymbol{r}) - \epsilon_{bg}(\boldsymbol{r}))/\epsilon_{bg}(\boldsymbol{r})$ is the contrast function, and $\epsilon(\boldsymbol{r})$ and $\epsilon_{bg}(\boldsymbol{r})$ denote the complex permittivities at position $\boldsymbol{r}$ with and without the target, respectively. As a physical constraint, the DIE in (1) must be satisfied in Ω_S and Ω_D. Thus, the CSI introduces the following cost function to reconstruct the contrast function $\chi(\omega; \boldsymbol{r})$:

$$\begin{aligned} F(\chi, w) &\equiv \frac{\sum_{\boldsymbol{r}_T} \left\| E^S(\omega; \boldsymbol{r}_T, \boldsymbol{r}_R) - \mathcal{G}^S[w] \right\|_{\Omega_S}^2}{\sum_{\boldsymbol{r}_T} \left\| E^S(\omega; \boldsymbol{r}_T, \boldsymbol{r}_R) \right\|_{\Omega_S}^2} \\ &+ \frac{\sum_{\boldsymbol{r}_T} \left\| \chi(\boldsymbol{r}) E^I(\omega; \boldsymbol{r}_T, \boldsymbol{r}') - w(\omega; \boldsymbol{r}_T, \boldsymbol{r}) + \chi(\boldsymbol{r}) \mathcal{G}^D[w] \right\|_{\Omega_D}^2}{\sum_{\boldsymbol{r}_T} \left\| \chi(\omega; \boldsymbol{r}) E^I(\omega; \boldsymbol{r}_T, \boldsymbol{r}') \right\|_{\Omega_D}^2}. \end{aligned} \quad (2)$$

Here, $\mathcal{G}^S$ and $\mathcal{G}^D$ are defined as

$$\mathcal{G}^S[w] = k_{bg}^2 \int_{\Omega_D} G^{bg}(\omega; \boldsymbol{r}_R, \boldsymbol{r}) w(\omega; \boldsymbol{r}_T, \boldsymbol{r}) d\boldsymbol{r}, \quad (\boldsymbol{r}_R \in \Omega_S) \quad (3)$$

$$\mathcal{G}^D[w] = k_{bg}^2 \int_{\Omega_D} G^{bg}(\omega; \boldsymbol{r}', \boldsymbol{r}) w(\omega; \boldsymbol{r}_T, \boldsymbol{r}) d\boldsymbol{r}, \quad (\boldsymbol{r}' \in \Omega_D). \quad (4)$$

$\|\cdot\|_{\Omega_S}^2$ and $\|\cdot\|_{\Omega_D}^2$ express the l_2 norms calculated in Ω_S and Ω_D, respectively. By sequentially updating $w(\omega; \boldsymbol{r}_T, \boldsymbol{r})$, $E^T(\omega; \boldsymbol{r}_T, \boldsymbol{r}_R)$, and $\chi(\omega; \boldsymbol{r})$ (primary unknowns), $F(\chi, w)$ is minimized, and the variable for the total fields in the ROI, $E^T(\omega; \boldsymbol{r}_T, \boldsymbol{r}_R)$ (secondary unknowns), is also optimized during the CSI processing, which is distinctly characteristic of the CSI scheme.

III. Proposed Method

A. CSI Enhanced Confocal Imaging (Tomography → Radar)

The most used radar imaging approach is based on the CI scheme, which has been widely employed in microwave breast imaging [8], [9]. Although the CI could reconstruct the reflection coefficient profile with considerably less complexity,

compared with the IS approach, its reconstruction accuracy highly depends on the assumed propagation model, which is mostly set as homogeneous media with average dielectric breast profiles. However, in dealing with highly heterogeneous breast media, the aforementioned presumption generates a nonnegligible erroneous response because of a mismatch between real and assumed dielectric properties. Most studies assume that a clutter response such as skin reflection or heterogeneity-caused scattering is perfectly eliminated during the CI preprocessing, which is hardly possible realistically. This is because a skin reflection waveform generally depends on the breast shape (e.g., the curvature of the surface) or the distance between the element and the skin surface (dielectric coupling effect), which has been demonstrated in some works in [36], [37], and [38].

To address this, our previous study [13] developed a CSI-based CI scheme, which provides a good estimate of Green's function in an arbitrary heterogeneous model and generates an accurate clutter signal by exploiting the optimized total fields by the CSI. The methodology is as follows. First, we applied the CSI optimization scheme assuming the background media, such as skin, and adipose-dominant media, that is, only the total field, $E^{\mathrm{T}}(\omega; \boldsymbol{r}_{\mathrm{T}}, \boldsymbol{r})$ is updated using $\hat{\chi}(\omega; \boldsymbol{r})$, which is determined by the assumed background media. Thereafter, by exploiting the aforementioned optimized total field, the Green's function was determined as

$$\tilde{G}_{\mathrm{T}}^{\mathrm{bg}}(\omega; \boldsymbol{r}_{\mathrm{T}}, \boldsymbol{r}) \equiv \frac{\hat{E}^{\mathrm{T}}(\omega; \boldsymbol{r}_{\mathrm{T}}, \boldsymbol{r})}{E_{\mathrm{bg}}^{\mathrm{T}}(\omega; \boldsymbol{r}_{\mathrm{T}}, \boldsymbol{r}_{\mathrm{T}})} \tag{5}$$

$$\tilde{G}_{\mathrm{R}}^{\mathrm{bg}}(\omega; \boldsymbol{r}_{\mathrm{R}}, \boldsymbol{r}) \equiv \frac{\hat{E}^{\mathrm{T}}(\omega; \boldsymbol{r}_{\mathrm{R}}, \boldsymbol{r})}{E_{\mathrm{bg}}^{\mathrm{T}}(\omega; \boldsymbol{r}_{\mathrm{R}}, \boldsymbol{r}_{\mathrm{R}})} \tag{6}$$

where $E_{\mathrm{bg}}^{\mathrm{T}}(\omega; \boldsymbol{r}_{\mathrm{T}}, \boldsymbol{r}_{\mathrm{T}})$ and $E_{\mathrm{bg}}^{\mathrm{T}}(\omega; \boldsymbol{r}_{\mathrm{R}}, \boldsymbol{r}_{\mathrm{R}})$ express the total fields measured at $\boldsymbol{r}_{\mathrm{T}}$ from the source at $\boldsymbol{r}_{\mathrm{T}}$ and that measured at $\boldsymbol{r}_{\mathrm{R}}$ from the source at $\boldsymbol{r}_{\mathrm{R}}$, respectively. Also the division operator in (5) and (6) denotes the element-wise division operator along ω. The background media is assumed as a vacuum. $\hat{E}^{\mathrm{T}}(\omega; \boldsymbol{r}_{\mathrm{T}}, \boldsymbol{r})$ and $\hat{E}^{\mathrm{T}}(\omega; \boldsymbol{r}_{\mathrm{R}}, \boldsymbol{r})$ are the optimized total fields at $\boldsymbol{r}$ by the CSI with the fixed contrast function as $\hat{\chi}(\omega; \boldsymbol{r})$. In addition, $\hat{E}^{\mathrm{T}}(\omega; \boldsymbol{r}_{\mathrm{T}}, \boldsymbol{r})$ and $\hat{E}^{\mathrm{T}}(\omega; \boldsymbol{r}_{\mathrm{R}}, \boldsymbol{r})$ can be given by the reciprocity theorem since the transmitters and receivers are convertible.

In addition, the proposed scheme focuses on the following distinct advantages, in terms of clutter signal extraction and suppression. The CSI can provide the total fields in the ROI, which contributes to generating the total fields of the background media (skin and adipose dominant breast) excluding a high contrast object, $\tilde{E}^{\mathrm{TB}}(\omega; \boldsymbol{r}_{\mathrm{T}}, \boldsymbol{r}_{\mathrm{R}})$ as

$$\begin{aligned}&\tilde{E}^{\mathrm{TB}}(\omega; \boldsymbol{r}_{\mathrm{T}}, \boldsymbol{r}_{\mathrm{R}})\\ &\equiv E^{\mathrm{I}}(\omega; \boldsymbol{r}_{\mathrm{T}}, \boldsymbol{r}_{\mathrm{R}})\\ &\quad + k_{\mathrm{B}}^2 \int_{\Omega_{\mathrm{D}}} \tilde{G}_{\mathrm{R}}^{\mathrm{B}*}(\omega; \boldsymbol{r}, \boldsymbol{r}_{\mathrm{R}}) \tilde{w}(\omega; \boldsymbol{r}_{\mathrm{T}}, \boldsymbol{r}) d\boldsymbol{r}, \quad (\boldsymbol{r}_{\mathrm{R}} \in \Omega_{\mathrm{S}}).\end{aligned} \tag{7}$$

$\tilde{G}_{\mathrm{R}}^{\mathrm{B}*}(\omega; \boldsymbol{r}_{\mathrm{R}}, \boldsymbol{r})$ is Green's function in assuming the background media, given by (6). $\tilde{w}(\omega; \boldsymbol{r}_{\mathrm{T}}, \boldsymbol{r})$ expresses $\tilde{w}(\omega; \boldsymbol{r}_{\mathrm{T}}, \boldsymbol{r}) \equiv \hat{\chi}(\omega, \boldsymbol{r}) \hat{E}^{\mathrm{T}}(\omega; \boldsymbol{r}_{\mathrm{T}}, \boldsymbol{r})$, where $\hat{\chi}(\omega, \boldsymbol{r})$ is fixed. $\hat{E}^{\mathrm{T}}(\omega; \boldsymbol{r}_{\mathrm{T}}, \boldsymbol{r})$ is also provided by the optimization outputs, similar to (5) or (6). Then, the CI image $\tilde{I}(\boldsymbol{r})$ is defined as

$$\begin{aligned}\tilde{I}(\boldsymbol{r}) = \sum_{(\boldsymbol{r}_{\mathrm{T}}, \boldsymbol{r}_{\mathrm{R}}) \in \Omega_{\mathrm{S}}} \int_{-\infty}^{\infty} & E^{\mathrm{S}}(\omega; \boldsymbol{r}_{\mathrm{T}}, \boldsymbol{r}_{\mathrm{R}})\\ & \times \tilde{G}_{\mathrm{R}}^{\mathrm{bg}}(\omega; \boldsymbol{r}_{\mathrm{R}}, \boldsymbol{r}) \tilde{G}_{\mathrm{T}}^{\mathrm{bg}*}(\omega; \boldsymbol{r}_{\mathrm{T}}, \boldsymbol{r}) d\omega.\end{aligned} \tag{8}$$

Details of the aforementioned scheme have been previously described [13]. If we provide a previous background model constituting only skin and adipose tissue (low contrast), the above CI provides the reconstruction image focusing only on high-contrast tissues, such as fibroglandular or cancerous tissues. However, since the CI provides only a qualitative image, such as reflection strength, it is insufficient to discriminate the difference between fibroglandular and tumor tissues. Thus, the posttomography approach is essentially required for the quantitative reconstruction of complex permittivity to provide an accurate recognition rate between glandular and cancerous tissues.

B. Initial Estimate With Enhanced Confocal Image (Radar → Tomography)

To provide an appropriate initial estimation, this method converts the CI image into the dielectric profile, using the following deconvolution and optimization scheme. Fig. 2 illustrates the processing flow of the deconvolution scheme. First, to enhance the spatial resolution of the CI image, the following decomposition is introduced:

$$\hat{I}^{\mathrm{D}}(\boldsymbol{r}) = \iint_{-\infty}^{\infty} H(k_x, k_y; \sigma_{\mathrm{I}}; \alpha) e^{j(k_x x + k_y y)} dk_x dk_y \tag{9}$$

where $H(k_x, k_y; \sigma_{\mathrm{I}}; \alpha)$ is defined as

$$H(k_x, k_y; \sigma_{\mathrm{I}}; \alpha) = W^{\mathrm{Roff}}(k_x, k_y; \alpha) \frac{\tilde{I}(k_x, k_y)}{G(k_x, k_y; \sigma_{\mathrm{I}})} \tag{10}$$

where $\tilde{I}(k_x, k_y)$ denotes the 2-D Fourier transform of $\tilde{I}(\boldsymbol{r})$ in terms of x and y. $G(k_x, k_y; \sigma_{\mathrm{I}})$ is defined as

$$G(k_x, k_y; \sigma_{\mathrm{I}}) = \iint_{-\infty}^{\infty} \exp\left[-\frac{(x^2 + y^2)}{2\sigma_{\mathrm{I}}^2}\right] e^{-j(k_x x + k_y y)} dx dy \tag{11}$$

where σ_{I} denotes the standard deviation of the Gaussian point spread function. In addition, $W^{\mathrm{Roff}}(k_x, k_y; \alpha)$ is the roll-off filter-based windowing function as follows (12), shown at the bottom of the next page, where $k_r \equiv \sqrt{k_x^2 + k_y^2}$ holds. Parameters σ_{I} and α are determined by considering the point spread function and sidelobe level of the output image $\hat{I}^{\mathrm{D}}(\boldsymbol{r})$, assuming a single-point object in the background media.

The initial estimate of the Debye parameter profiles is determined as follows:

$$\boldsymbol{p}(\boldsymbol{r}; \beta) = \boldsymbol{p}_{\mathrm{B}}(\boldsymbol{r}) + \beta \tilde{I}(\boldsymbol{r}) \boldsymbol{p}_{\mathrm{tumor}} \tag{13}$$

where $\boldsymbol{p}_{\mathrm{canc}} \equiv (\epsilon_{\infty}^{\mathrm{tumor}}, \Delta\epsilon^{\mathrm{tumor}}, \sigma_{\mathrm{s}}^{\mathrm{tumor}})$ denotes the representative Debye parameter vector of the tumor tissue. $\boldsymbol{p}_{\mathrm{canc}}(\boldsymbol{r}) \equiv (\epsilon_{\infty}^{\mathrm{tumor}}, \Delta\epsilon^{\mathrm{tumor}}, \sigma_{\mathrm{s}}^{\mathrm{tumor}})$ is defined as

$$\boldsymbol{p}_{\mathrm{B}}(\boldsymbol{r}) \equiv \begin{cases} (\epsilon_{\infty}^{\mathrm{skin}}, \Delta\epsilon^{\mathrm{skin}}, \sigma_{\mathrm{s}}^{\mathrm{skin}}), & (\boldsymbol{r} \in \Omega_{\mathrm{skin}} \cap \Omega_{\mathrm{D}}) \\ (\epsilon_{\infty}^{\mathrm{adi}}, \Delta\epsilon^{\mathrm{adi}}, \sigma_{\mathrm{s}}^{\mathrm{adi}}), & (\boldsymbol{r} \in \overline{\Omega}_{\mathrm{skin}} \cap \Omega_{\mathrm{D}}). \end{cases} \tag{14}$$

Notably, since we assume that the background media are composed of only skin and adipose tissue, the parameters for fibroglandular or cancer tissues are not required here.

The parameter β is then optimized as

$$\hat{\beta} = \arg\min_{\beta} F(\chi(\boldsymbol{p}(\boldsymbol{r}; \beta)), \omega). \tag{15}$$

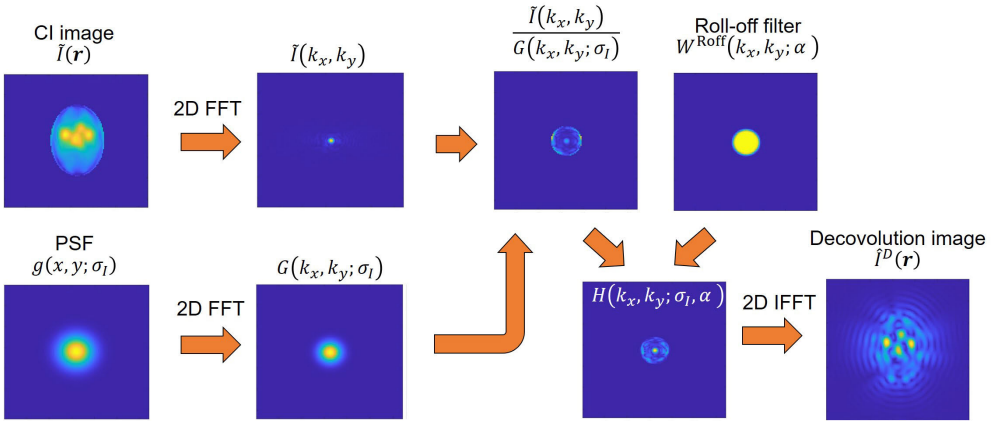

Fig. 2. Deconvolution process using the 2-D Gaussian function and roll-off filtering in the proposed method.

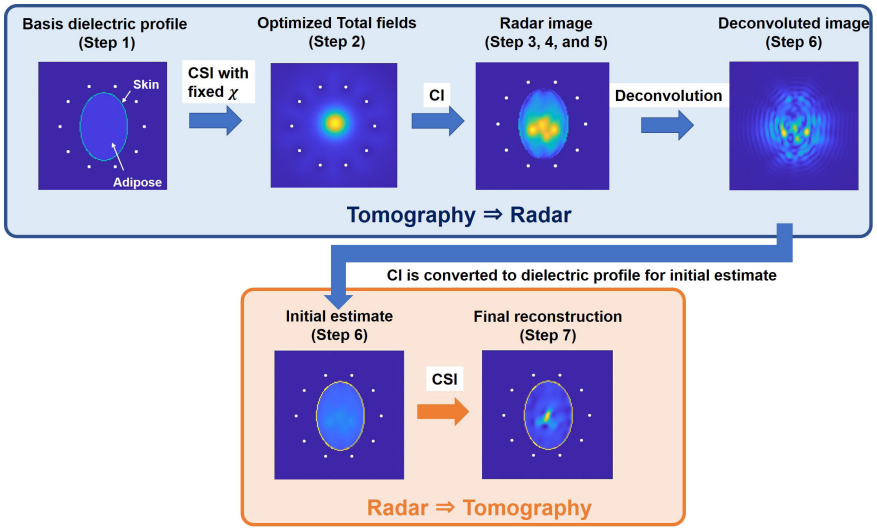

Fig. 3. Schematic of the proposed method. Bidirectional processing between radar and tomography.

Here, $\chi(\boldsymbol{p}(\boldsymbol{r};\beta))$ denotes the contrast function, which is defined by the given Debye profile $\boldsymbol{p}(\boldsymbol{r};\beta)$. Finally, the initial estimate is determined as $\chi(\boldsymbol{p}(\boldsymbol{r};\hat{\beta}))$, and the CSI iteration process is conducted with N iterations to provide a final reconstruction profiles of the complex permittivity. Note that this study does not focus on the resolution enhancement for the CI images, but aims to provide an accurate initial estimate using higher resolutions and more accurate CI profiles, for the postquantitative imaging with CSI.

C. Procedure of Proposed Method

Fig. 3 shows the schematic of the proposed method, namely, the bidirectional processing between radar and tomography. The procedure of this method is as follows.

Step 1: The dielectric profile using only skin and adipose media is defined in (14) as $\boldsymbol{p}_{\mathrm{B}}(\boldsymbol{r})$, and $\chi^{\mathrm{low}}(\omega, \boldsymbol{r})$ is also defined using this profile as $\boldsymbol{p}_{\mathrm{B}}(\boldsymbol{r})$, assuming that the background media is a vacuum.

Step 2: $\hat{E}^{\mathrm{T}}(\omega; \boldsymbol{r}_{\mathrm{T}}, \boldsymbol{r})$ is optimized at each angular frequency ω, by minimizing the CSI cost function in (2), where $\chi^{\mathrm{low}}(\omega, \boldsymbol{r})$ is fixed in the iteration process.

Step 3: Green's functions, $\tilde{G}^{\mathrm{B}}_{\mathrm{T}}(\omega; \boldsymbol{r}_{\mathrm{T}}, \boldsymbol{r})$ and $\tilde{G}^{\mathrm{B}}_{\mathrm{R}}(\omega; \boldsymbol{r}_{\mathrm{R}}, \boldsymbol{r})$, are determined in (5) and (6), respectively, by the updated total field as $\hat{E}^{\mathrm{T}}(\omega_i; \boldsymbol{r}_{\mathrm{T}}, \boldsymbol{r})$.

Step 4: The clutter signal, $\tilde{E}^{\mathrm{TB}}(\omega_i; \boldsymbol{r}_{\mathrm{T}}, \boldsymbol{r}_{\mathrm{R}})$, is generated by ((7)) and is eliminated from the scattered signal. The scattered field is determined, assuming a multilayered background $\tilde{E}^{\mathrm{S}}(\omega_i; \boldsymbol{r}_{\mathrm{T}}, \boldsymbol{r}_{\mathrm{R}})$.

Step 5: The CSI-enhanced CI process is conducted using (8) and generates the image as $\tilde{I}(\boldsymbol{r})$.

Step 6: Image deconvolution is applied in (9), and the initial estimate for the Debye parameters are determined as $\chi(\boldsymbol{p}(\boldsymbol{r};\hat{\beta}))$ using (15).

$$W^{\mathrm{Roff}}(k_x, k_y; \alpha) = \begin{cases} 1, & (0 \le k_r \le (1-\alpha)k_r^{\mathrm{th}}) \\ \dfrac{1}{2}\left\{1 - \sin\left(\dfrac{\pi(k_r - k_r^{\mathrm{th}})}{2\alpha k_r^{\mathrm{th}}}\right)\right\}, & ((1-\alpha)k_r^{\mathrm{th}} < k_r \le (1+\alpha)k_r^{\mathrm{th}}) \\ 0, & (k_r > (1+\alpha)k_r^{\mathrm{th}}) \end{cases} \tag{12}$$

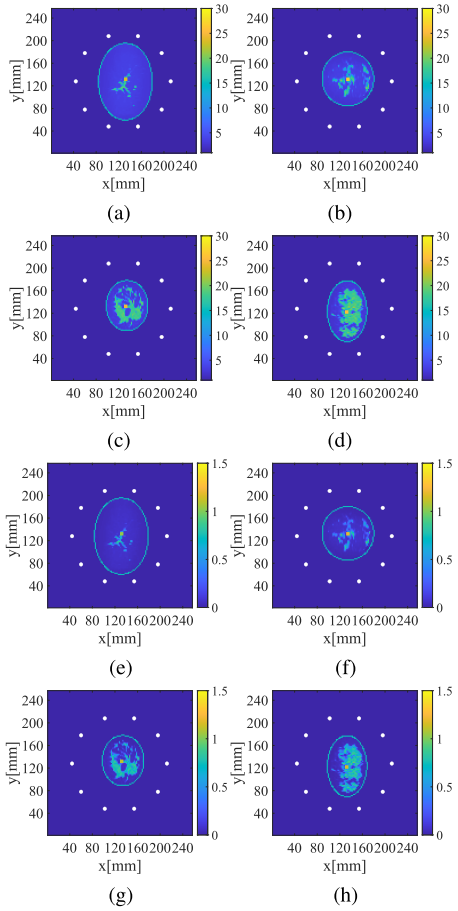

Fig. 4. Ground-truth profiles of Debye parameters ϵ_∞ and σ_s in each class. White dots denote the transmitters and receivers. (a) ϵ_∞ of Class 1. (b) ϵ_∞ of Class 2. (c) ϵ_∞ of Class 3. (d) ϵ_∞ of Class 4. (e) σ_s of Class 1. (f) σ_s of Class 2. (g) σ_s of Class 3. (h) σ_s of Class 4.

Step 7: Using the initial estimate, $\chi(\boldsymbol{p}(\boldsymbol{r};\hat{\beta}))$, CSI is applied and affords the final reconstruction profile of complex permittivity.

Notably, Step 3 generates the accurate propagation model for heterogeneous media, and Step 4 introduces the suppression process for the clutter from the skin surface.

IV. Numerical Test

A. Numerical Setup

The 2-D FDTD-based numerical investigations are described as follows. This simulation introduces the four types of MRI-derived phantoms as—Class 1 (mostly fatty, ID = 012804), Class 2 (scattered fibroglandular, ID = 070604PA1), Class 3 (heterogeneously dense, ID = 062204), and Class 4 (very dense, ID = 012304)—which are available from published repositories [39]. The frequency dispersion model is expressed as the single-pole Debye as follows:

$$\epsilon_{\text{Debye}}(\omega;\epsilon_\infty,\Delta\epsilon,\sigma_s)=\varepsilon_\infty+\frac{\Delta\varepsilon}{1+j\omega\tau}+\frac{\sigma_s}{j\omega\varepsilon_0} \tag{16}$$

where τ is the relaxation time and is fixed at $\tau = 1.5\times10^{-11}$ s. The main Debye parameters $(\epsilon_\infty,\Delta\epsilon,\sigma_s)$ could be accurately associated with the MRI image via piecewise linear mapping [40]. Then, the scattered data are generated using the 2-D FDTD, where the above single-pole Debye dispersion model is introduced. Fig. 4 illustrates the spatial profile for

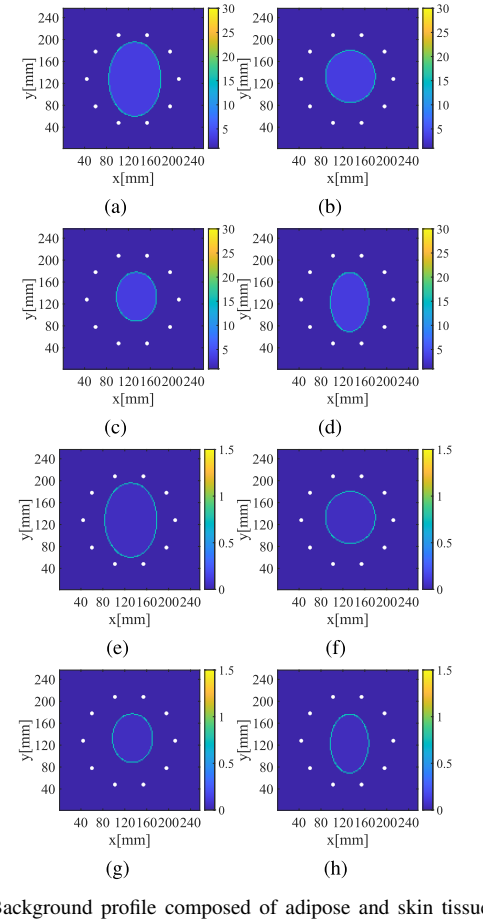

Fig. 5. Background profile composed of adipose and skin tissue as to the Debye parameters ϵ_∞ and σ_s in each class. White dots denote the transmitters and receivers. (a) ϵ_∞ of Class 1. (b) ϵ_∞ of Class 2. (c) ϵ_∞ of Class 3. (d) ϵ_∞ of Class 4. (e) σ_s of Class 1. (f) σ_s of Class 2. (g) σ_s of Class 3. (h) σ_s of Class 4.

TABLE I
DEBYE PARAMETERS FOR EACH TISSUE

Tissue type	ϵ_∞	$\Delta\epsilon$	σ_s [S/m]
Skin	15.9	23.8	0.83
Adipose (median)	3.1	1.6	0.05
Fibroglandular (median)	13.8	35.6	0.74
Fibroglandular (high)	18.3	43.0	1.08
Cancer	22.0	51.6	1.30

two of the Debye parameters as ϵ_∞ and σ_s of four different phantoms, and Table I shows the assumed range for the Debye parameters of each tissue, which is dependent on the associated MRI image strength. Cancerous tissue with dimensions of 6 × 6 mm is located at the center of each phantom, with the Debye parameters of $(\epsilon_\infty,\Delta\epsilon,\sigma_s) = (22.0, 51.6, 1, 3)$, derived from a previous study [40]. The ten transmitters (ideal point sources) and receivers configure a circular array, and all their combination data are input into the inversion scheme. The Gaussian modulated pulse with 1.27-GHz center frequency and 1.91-GHz bandwidth is excited as the source current. All the cell sizes of the FDTD, CI, and CSI are unified as 2 mm, where the FDTD code was modified from the original in-house code by the University of Wisconsin–Madison, Madison, WI, USA.

B. Results: Tomography → Radar (CSI-Enhanced CI)

First, the CI image reconstruction is presented. We first assume a noiseless situation to assess the systematical error in

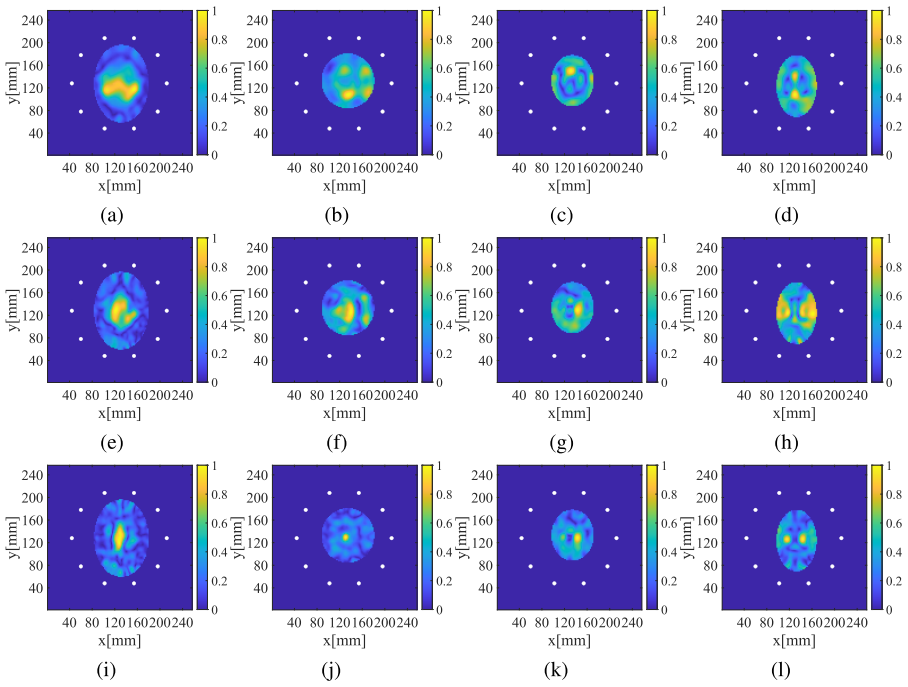

Fig. 6. Reconstruction images by the conventional CI method for each class at the two conditions. (a) Class 1: $\epsilon_{bg} = 6$. (b) Class 2: $\epsilon_{bg} = 6$. (c) Class 3: $\epsilon_{bg} = 6$. (d) Class 4: $\epsilon_{bg} = 6$. (e) Class 1: $\epsilon_{bg} = 8$. (f) Class 2: $\epsilon_{bg} = 8$. (g) Class 3: $\epsilon_{bg} = 8$. (h) Class 4: $\epsilon_{bg} = 8$. (i) Class 1: $\epsilon_{bg} = 10$. (j) Class 2: $\epsilon_{bg} = 10$. (k) Class 3: $\epsilon_{bg} = 10$. (l) Class 4: $\epsilon_{bg} = 10$.

each process. For the method comparison, the traditional CI results are introduced, which assumes that the breast media forms a homogeneous profile with the representative complex permittivity [13]. Here, for clutter suppression in the traditional and proposed CI schemes, we assume a simple breast model comprising only skin and adipose media, as shown in Fig. 5. Fig. 6 shows the results obtained from the CI images, where the three different relative permittivities are assumed to be $\epsilon_{bg} = 6, 8$, and 10, because the reconstruction accuracy of the CI image is mostly dependent on the relative permittivity ϵ_{bg}, which is converted to the propagation speed v_{bg} in the breast media as $v_{bg} = v_{air}/\sqrt{\epsilon_{bg}}$ with that in the air as v_{air}. Here, all the imaging areas, in Fig. 6, are truncated on the boundary between the skin of the breast and air. Notably, in the traditional CI image, the clutter signal from the background media (see Fig. 5), is generated in the FDTD, and eliminated. As shown in Fig. 6, the traditional CI image could not provide an accurate location or area of the high contrast object of fibro-glandular or cancer tissues, which are mainly caused by a mismatch in the relative permittivity.

Next, the reconstruction results of the CSI-enhanced CI are presented as follows. In this case, we investigate the two conditions, with regard to the calculation of Green's function in (5) and (6) and the clutter suppression in (7). In Cond. I, the total fields $\hat{E}^{T}(\omega, \boldsymbol{r}; \boldsymbol{r}_T)$ and the scattered fields $\tilde{E}^{S}(\omega; \boldsymbol{r}_T, \boldsymbol{r}_R)$ are given by the FDTD method, that is, the ideal case, where referential information is input to the enhanced SAR reconstruction in (8). On the contrary, in Cond. II, $\tilde{E}^{S}(\omega; \boldsymbol{r}_T, \boldsymbol{r}_R)$ and $\hat{E}^{T}(\omega, \boldsymbol{r}; \boldsymbol{r}_T)$ are calculated by the optimization output of the CSI. Here, the convergence criteria of the above CSI process is determined by the maximum iteration number, which is set to 1000 in this case. Table II summarizes the definitions of these conditions. Fig. 7 illustrates the reconstruction results of the total fields in the ROI cells at the specific transmitter, compared with the FDTD data, and it demonstrates that

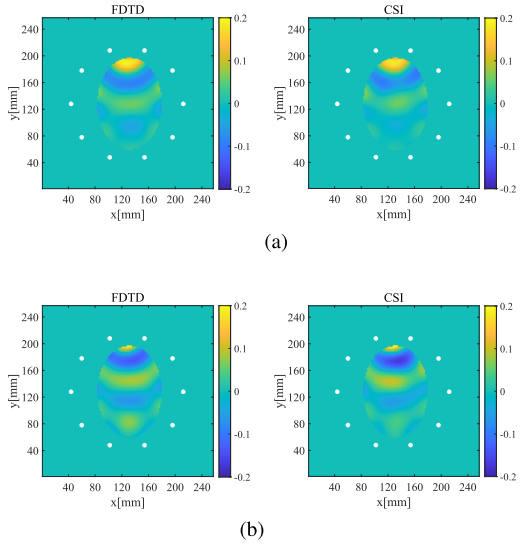

Fig. 7. Reconstruction profile of the total field in the ROI area at the specific transmitter at Class 1 and the frequency at 1.27 GHz. (a) Real part. (b) Imaginary part.

TABLE II
DETAILS OF EACH CONDITION OF THE PROPOSED METHOD

	Green's functions in (5) and (6))	Total fields in (7)
Cond. I	FDTD	FDTD
Cond. II	CSI	CSI

the CSI can optimize the total field in all ROI cells with considerable similarity to that provided by the FDTD (i.e., reference data). Thus, Green's functions in (5) and (6) could be accurately provided for post-CI processes.

Next, Fig. 8 shows the reconstruction results using the proposed method in both Cond. I and II, where each imaging

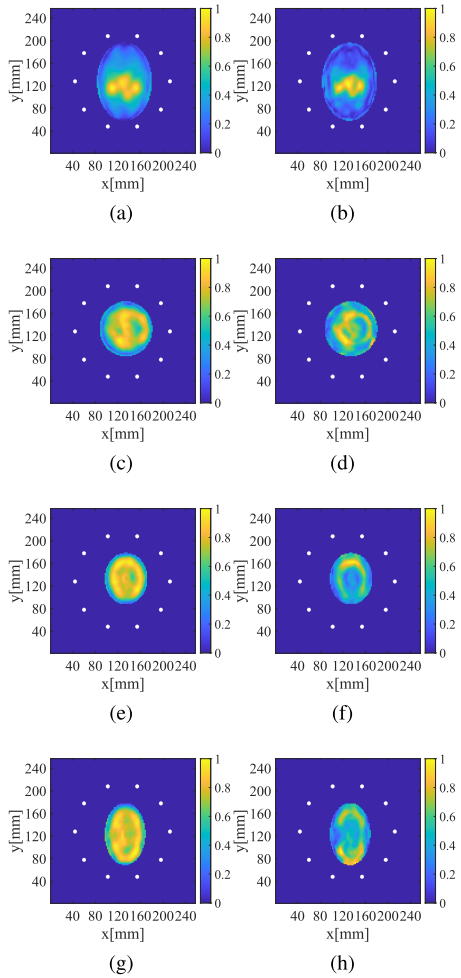

Fig. 8. Reconstruction images by the proposed CI method for each class at the two conditions. (a) Class 1: Cond. I. (b) Class 1: Cond. II. (c) Class 2: Cond. I. (d) Class 2: Cond. II. (e) Class 3: Cond. I. (f) Class 3: Cond. II. (g) Class 4: Cond. I. (h) Class 4: Cond. II.

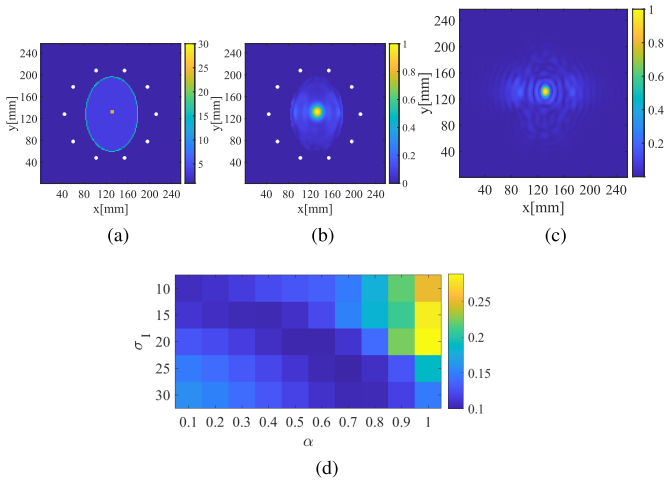

Fig. 9. Determination of the optimal α and σ_I by evaluating the point-spread function. (a) True ϵ_∞. (b) CI w/o deconv. (c) CI w/ deconv. (d) $\mathrm{Err}_{\mathrm{CI}}(\sigma_I, \alpha)$.

area is truncated on the boundary between the skin of the breast and air. As shown in the results in Fig. 8, the proposed CI schemes reconstruct the high energy around the boundary area between the adipose and fibroglandular areas, because

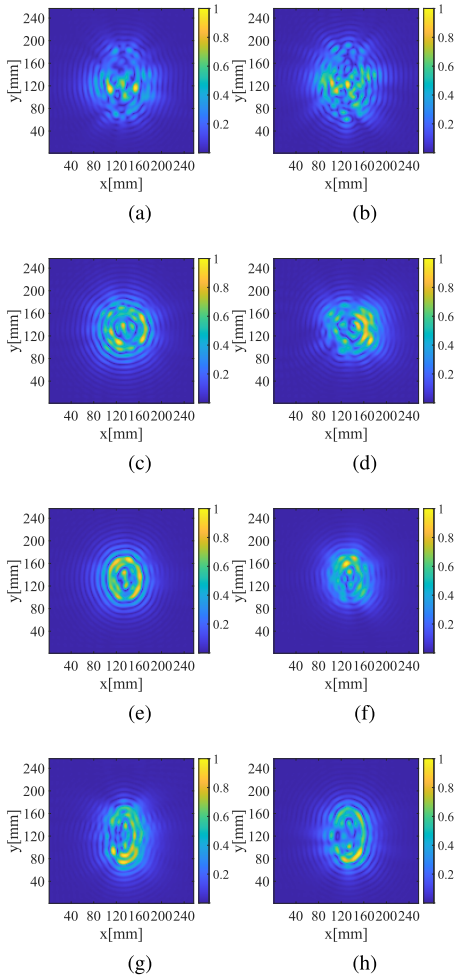

Fig. 10. Deconvolution results of the CSI-enhanced CI images for each class. First column: Cond. I. Second column: Cond. II. (a) and (b) Class 1. (c) and (d) Class 2. (e) and (f) Class 3. (g) and (h) Class 4.

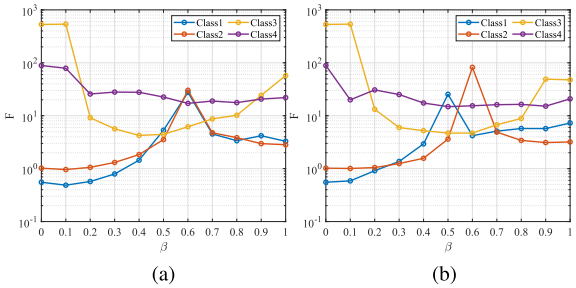

Fig. 11. Cost function as a function of β in each class. (a) Cond. I. (b) Cond. II.

the main reflection inside the breast is caused by the contrast between these tissues. Although the cancerous tissues are buried in the responses of the fibroglandular area, it provides an appropriate initial estimate for the post-CSI quantitative imaging to distinguish the tumor and fibro-tissues based on the dielectric profile. In addition, the CI images in Cond. II has a differential response from Cond. I, that is, the referential CI image, because of inaccuracy in generating the total field in the ROI area. These differences are more distinct in the dense cases, such as Class 3 or 4, and this is because a high contrast profile requires more iteration numbers to reach a certain accuracy of total field optimization.

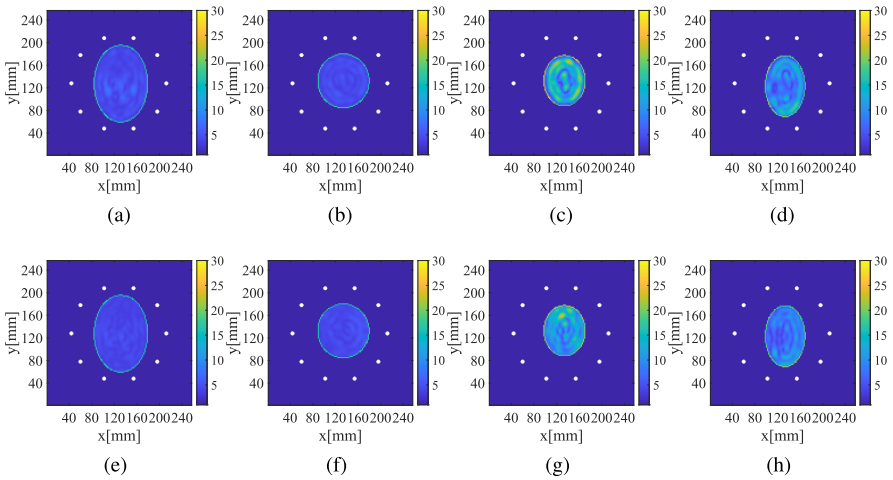

Fig. 12. Initially estimated permittivity profile as to ϵ_∞ for each class and condition. (a) Class 1 (Cond. I). (b) Class 2 (Cond. I). (c) Class 3 (Cond. I). (d) Class 4 (Cond. I). (e) Class 1 (Cond. II). (f) Class 2 (Cond. II). (g) Class 3 (Cond. II). (h) Class 4 (Cond. II).

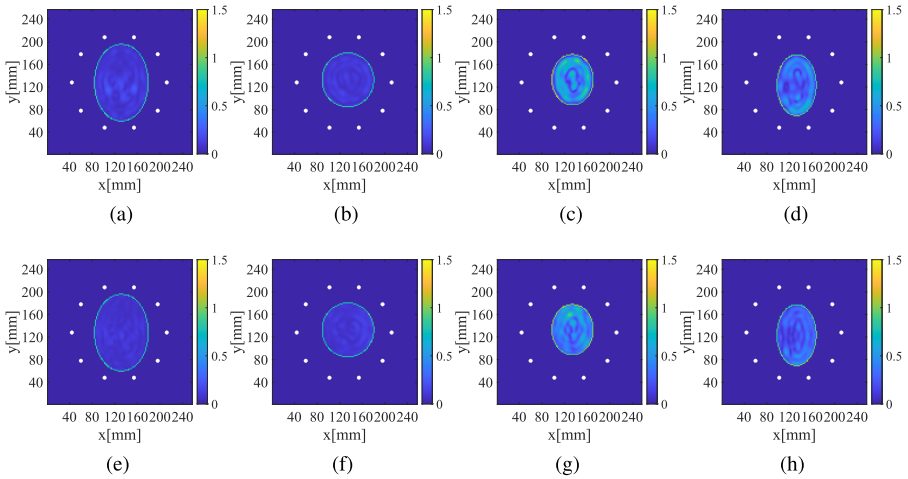

Fig. 13. Initially estimated permittivity profile as to σ_s for each class and condition. (a) Class 1 (Cond. I). (b) Class 2 (Cond. I). (c) Class 3 (Cond. I). (d) Class 4 (Cond. I). (e) Class 1 (Cond. II). (f) Class 2 (Cond. II). (g) Class 3 (Cond. II). (h) Class 4 (Cond. II).

C. Results: Radar → Tomography (CI-Enhanced CSI)

1) Deconvolution Results: Here, the CI-enhanced CSI approach is investigated as follows. First, the initial estimate scheme using the CI image with the Gaussian function-based deconvolution is assessed as follows. In this case, parameters σ_I and α used in (9) are optimized under the criteria with the following root mean square error (RMSE) between the ground-truth profile and the output CI images as

$$\mathrm{Err}_{\mathrm{CI}}(\sigma_I, \alpha) = \frac{1}{N_I}\sqrt{\frac{\sum_{i=1}\left|I_{\mathrm{true}}(\boldsymbol{r}_i) - \tilde{I}(\boldsymbol{r}_i)\right|^2}{\sum_{i=1}|I_{\mathrm{true}}(\boldsymbol{r}_i)|^2}}. \tag{17}$$

Although the metric $\mathrm{Err}_{\mathrm{CI}}(\sigma_I, \alpha$ does not directly evaluate the spatial resolution of the radar image, it can assess the accuracy of the initial estimate of the post-CSI processing, that is, the similarity to the actual dielectric profile. Fig. 9 shows the evaluations of the aforementioned errors $\mathrm{Err}_{\mathrm{CI}}(\sigma_I, \alpha)$ as a function of σ_I and α assuming that the single point-shape object $(\epsilon_\infty, \Delta\epsilon, \sigma_s) = (23.3, 43.0, 1.03)$ is located in the center of the breast with a skin-adipose-based background in Class 1. This figure shows that there is an optimal combination of these parameters at the minimal RMSE, and we determine that the optimal parameters of $\hat{\sigma}_I$ and $\hat{\alpha}$ are 50 mm and 0.7, respectively. Note that, this target model corresponds to the PSF. While we cannot optimize the parameters for unknown arbitrary breast profiles, a general radar image, including a response from fibroglandular or cancer tissues, is generally approximated as a convolution image between the actual contrast function profile $\chi(\boldsymbol{r})$ and the PSF. Thus, we use the optimal parameter in assuming the above PSF model in the following analysis. Fig. 10 shows the deconvolution results of the CI images of Fig. 8 using the optimal parameters of $\hat{\sigma}_I$ and $\hat{\alpha}$ for both Conditions I and II. The results in Fig. 10 demonstrate that the deconvolution scheme in Section III-B successfully upgrades the spatial resolution of the CI images, which contributes to the postinitial estimation process. However, some sidelobe responses appeared outside area of the breast area, which could be truncated from the ROI. In addition, this approach is based on linear approximation, and there are also some unnecessary responses due to the nonlinear effect.

2) Reconstruction Results: As the next step described in 15, the initial estimate for the post-CSI reconstruction is determined using the deconvoluted CI image as in Fig. 10. Fig. 11 shows the minimized CSI cost function for each selected β defined in (15) for each condition. Table III summarizes the

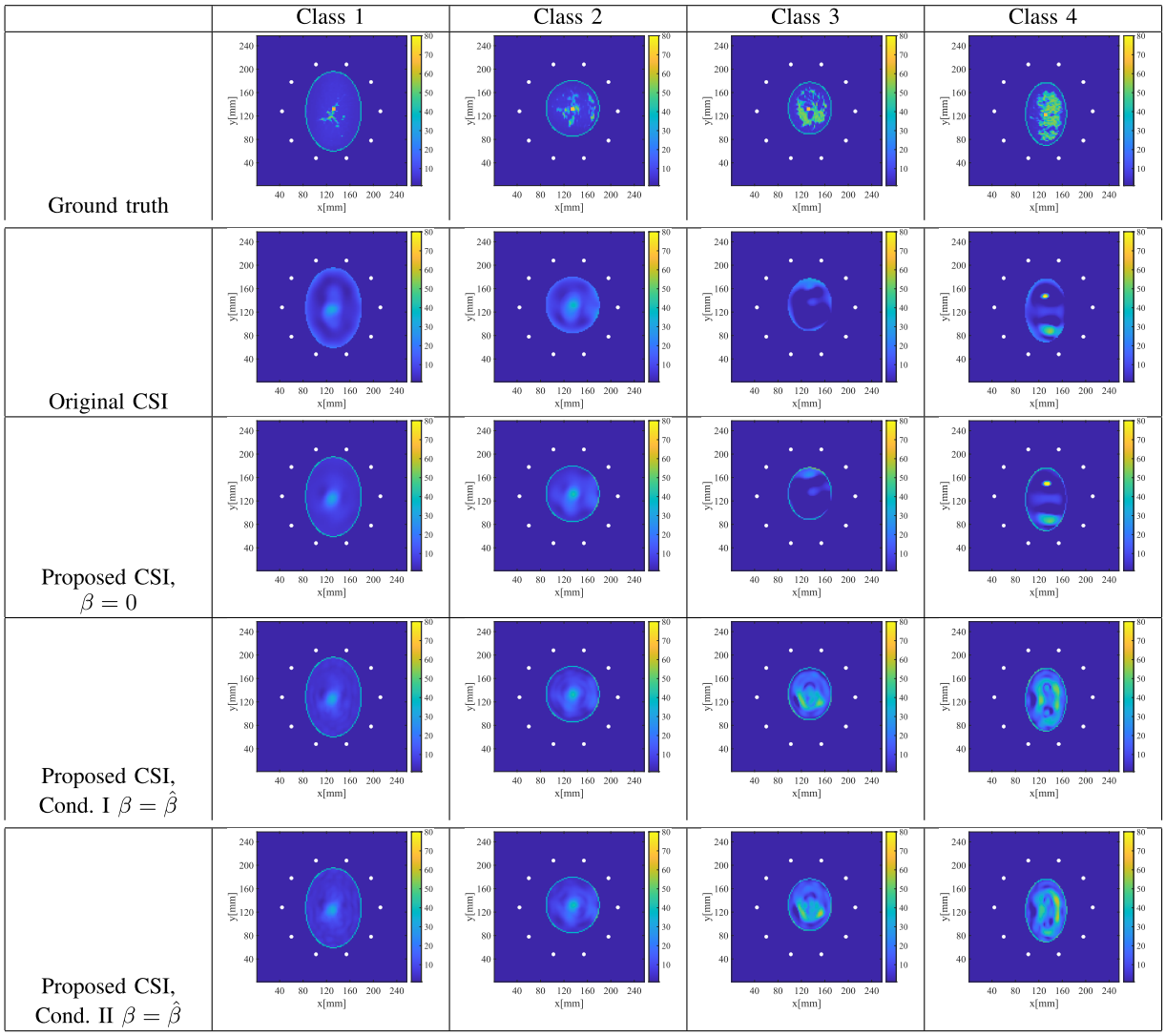

Fig. 14. Reconstruction results for the real part of the complex permittivity at 1.27 GHz in each method and class.

TABLE III

OPTIMIZED β IN DETERMINING THE INITIAL ESTIMATE WITH CSI COST FUNCTION

	Class 1	Class 2	Class 3	Class 4
Cond. I	0.1	0.1	0.4	0.6
Cond. II	0.1	0.1	0.5	0.5

optimized parameters $\hat{\beta}$ using 15 in each class. In the case of Class 1 or 2, namely, the lower density of the fibroglandular area, a low β is selected as the optimal value because the adipose area with a low dielectric contrast is dominant in either class. Contrarily, focusing on Class 3 or 4, that is, highly heterogeneous media, a high β becomes optimal because the initial estimate should have a high contrast profile, and those effects are almost common in Cond. I and II.

Figs. 12 and 13 show the initial estimate using each $\hat{\beta}$ in (13), as to the two of Debye parameters as ϵ_∞ and σ_s, respectively. Figs. 12 and 13 show that the proposed scheme could provide an appropriate initial estimate in each class, which is exploited in the CSI reconstruction. Figs. 14 and 15 show the reconstruction results of complex permittivity for real and imaginary parts, respectively, in each method, and condition. Focusing on the result in the original CSI, that is, without using the CI-based initial estimate, it considerably suffers from inaccuracy, especially in highly heterogeneous models such as Class 3 or 4, because the optimized solution in the original CSI would fall into the local optimal by starting from vacuum-based initial estimates, and could not reach the global optimum, particularly for the area with high contrast function. The results in Figs. 14 and 15 also confirm that the accuracy of the reconstruction results using the proposed method is significantly enhanced by those obtained using the original CSI scheme, by starting from a more accurate initial estimate, especially in Classes 3 and 4. Tables IV and V show the quantitative error analysis for the reconstruction results, with the RMSEs for each real and imaginary part of the complex permittivity at 1.27 GHz. The results in Tables IV and V also demonstrated that the proposed approach considerably suppresses the RMSE values. Note that, the accuracy improvement in Class 1 and 2 is limited compared with those obtained in the case of $\beta = 0$, because it starts the initial estimate with lower β as in Table III. On the contrary, in the cases of Class 3 or 4, namely, a highly heterogeneous profile, the initial

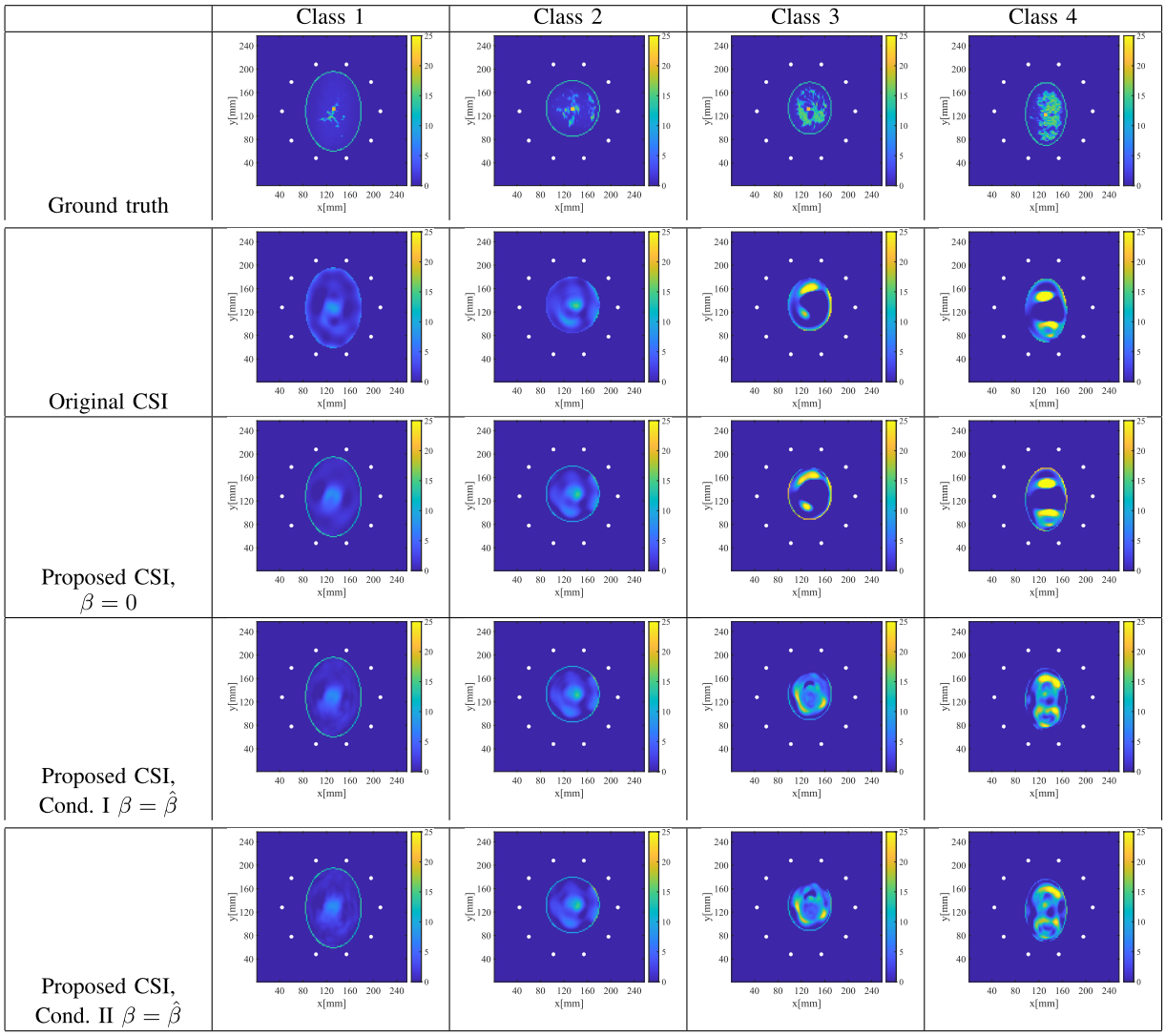

Fig. 15. Reconstruction results for the imaginary part of the complex permittivity at 1.27 GHz in each method and class.

TABLE IV

RMSE OF REAL PART OF COMPLEX PERMITTIVITY AT 1.27 GHz, IN EACH CLASS AND METHOD

	Original CSI	Proposed CSI		
		$\beta = 0$	Cond. I $\beta = \tilde{\beta}$	Cond. II $\beta = \tilde{\beta}$
Class 1	8.82	5.16	5.13	5.18
Class 2	10.89	8.14	8.08	8.21
Class 3	24.56	23.50	12.67	12.71
Class 4	25.86	24.52	16.50	15.30

TABLE V

RMSE OF THE IMAGINARY PART OF COMPLEX PERMITTIVITY AT 1.27 GHz, IN EACH CLASS AND METHOD

	Original CSI	Proposed CSI		
		$\beta = 0$	Cond. I $\beta = \tilde{\beta}$	Cond. II $\beta = \tilde{\beta}$
Class 1	2.98	1.80	1.71	1.72
Class 2	4.08	3.18	3.01	3.08
Class 3	9.59	9.52	6.44	6.70
Class 4	18.1	20.08	8.68	8.03

estimate with higher β contributes to accuracy improvement, compared with those obtained by $\beta = 0$, that is, the advantage of the processing in Section III-B.

3) Error Analysis: As another quantitative analysis, the correlation coefficients, denoted as ρ_{re} and ρ_{im} between true and reconstructed profiles, for both real and imaginary parts of complex permittivity, are introduced as

$$\rho_{\text{re}} = \frac{\boldsymbol{\epsilon}^{\Re}_{\text{true}} \cdot \boldsymbol{\epsilon}^{\Re}_{\text{est}}}{\left\|\boldsymbol{\epsilon}^{\Re}_{\text{true}}\right\| \left\|\boldsymbol{\epsilon}^{\Re}_{\text{true}}\right\|} \tag{18}$$

$$\rho_{\text{im}} = \frac{\boldsymbol{\epsilon}^{\Im}_{\text{true}} \cdot \boldsymbol{\epsilon}^{\Im}_{\text{est}}}{\left\|\boldsymbol{\epsilon}^{\Im}_{\text{true}}\right\| \left\|\boldsymbol{\epsilon}^{\Im}_{\text{true}}\right\|} \tag{19}$$

where $\boldsymbol{\epsilon}^{\Re}_{\text{true}}$ and $\boldsymbol{\epsilon}^{\Re}_{\text{est}}$ denote the spatial profile of the real part of complex permittivity of the ground truth and reconstructed images, respectively. $\boldsymbol{\epsilon}^{\Im}_{\text{true}}$ and $\boldsymbol{\epsilon}^{\Im}_{\text{est}}$ also denote those of the imaginary parts of complex permittivity of the ground truth and reconstructed images, respectively. The indexes ρ_{re} and ρ_{im} quantitatively assess the similarity between true and estimated profiles, especially for a similarity of area with higher contrast, that is, cancer and fibroglandular area.

TABLE VI

ρ_{re} AT 1.27 GHz, IN EACH CLASS AND METHOD

	Original CSI	Proposed CSI		
		$\beta = 0$	Cond. I $\beta = \tilde{\beta}$	Cond. II $\beta = \tilde{\beta}$
Class 1	0.553	0.873	0.875	0.873
Class 2	0.574	0.790	0.793	0.785
Class 3	-0.060	0.213	0.743	0.740
Class 4	0.098	0.300	0.563	0.637

TABLE VII

ρ_{im} AT 1.27 GHz, IN EACH CLASS AND METHOD

	Original CSI	Proposed CSI		
		$\beta = 0$	Cond. I $\beta = \tilde{\beta}$	Cond. II $\beta = \tilde{\beta}$
Class1	0.563	0.867	0.881	0.880
Class2	0.404	0.689	0.726	0.714
Class3	0.094	0.235	0.368	0.320
Class4	0.083	0.214	0.254	0.227

Tables VI and VII show the evaluations of ρ_{re} and ρ_{im} for each method and demonstrate that our proposed scheme significantly enhances the similarity of the dielectric profile, compared with those obtained by the original CSI scheme and the case without using the CI image ($\beta = 0$) in the initial estimate, in particular, of Class 3 or 4. There are some negative values in ρ_{re} (e.g., the original CSI in Table VI), and it is predicted that there are many cells with an inverse relationship between true and reconstructed dielectric properties. Note that the accuracy of the imaginary part in Class 3 or 4 is relatively lower than that of the real part. This is because these classes have high lossy media with densely distributed fibroglandular tissues, which makes it difficult to extract the scattered signal from the deeper area of breast media.

4) Case for Different Cancer Locations: Notably, our proposed scheme does not assume nor use prior knowledge of the cancer location. To demonstrate the above, we investigate the cases with different cancer cell locations located at off-center areas of the breast. Here, as a representative model for lowly and highly dense breasts, Classes 1 and 4 are investigated as follows. Fig. 16 shows the reconstruction results of the CSI-enhanced CI image and its deconvolution image, which could offer accurate focus on the actual cancer positions, especially for the Class 1 model. Fig. 17 also shows the reconstruction results obtained by the original CSI (without CI prior) and the proposed CSI method, where Condition II is assumed. In this case, the optimized β for Classes 1 and 4 are 0.1 and 0.6, respectively. Table VIII also shows the RMSE and ρ at the off-centered cancer case. These results demonstrated that our proposed scheme applies to different locations of the cancer tissues, as any prior knowledge of the cancer location is not used in either the CI or CSI processing schemes.

D. Case for Additive Noise

In this section, the case with additive noise is investigated to assess the sensitivity to noisy components. In this simulation model, the cell sizes in both the forward and inverse problems are set to the same dimension as 2 mm, which might incur the so-called inverse crime as in [41]. However, in some previous works [41], this issue would be mitigated, by considering the situation with additive noise as follows. White Gaussian noises

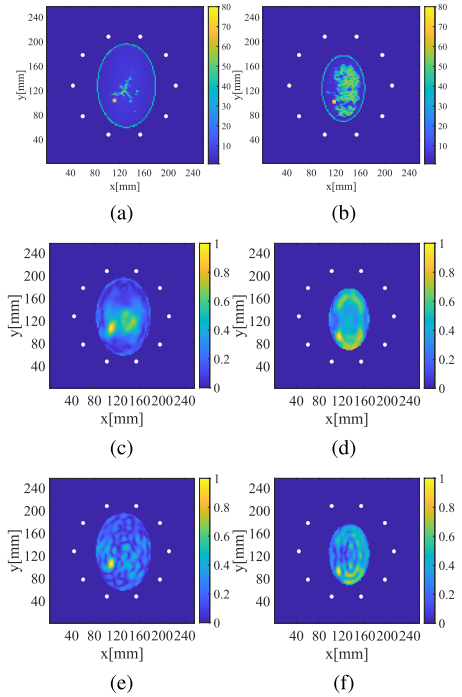

Fig. 16. Reconstruction results for CI and CSI images at 1.27 GHz in each method at the case for off-center located cancer. First column: Class 1. Second column: Class 4. (a) and (b) Ground truth. (c) and (d) CI. (e) and (f) Deconv. CI.

TABLE VIII

RMSE AND ρ IN EACH CLASS AND METHOD AT THE OFF-CENTERED CANCER CASE

	Class	RMSE		ρ	
		$\Re[\epsilon]$	$\Im[\epsilon]$	$\Re[\epsilon]$	$\Im[\epsilon]$
Original CSI	Class 1	8.96	3.08	0.54	0.52
	Class 4	25.99	17.26	0.14	0.15
Proposed CSI	Class 1	5.41	1.67	0.86	0.87
	Class 4	14.50	7.67	0.68	0.27

are added to the observed total fields in the time domain. The signal-to-noise ratio (SNR) is determined as the ratio of maximum signal-to-noise power (variance of the Gaussian distribution, and the signal includes reflection responses from the skin surface, which would be much stronger than those from the inner area of the breast, such as fibroglandular, or cancer tissues, because we do not assume a matching coupling media to suppress the skin reflection. As in Section IV-C4, the two representative cases Class 1 and 4 are investigated as follows. We assume the two cases as having SNR values of 30 and 40 dB, respectively. While these SNR levels are apparently high, they are available in the actual measurement scenario, such as in [38], Fig. 18 shows an example of the received signal assuming the Class 1 at each SNR level, where the responses with, or without skin reflection elimination are illustrated for a noise-free situation. This figure shows that the response from the inner area (yellow) is considerably less than that of skin reflection (red) and is buried into the noise component, especially for an SNR of 30 dB. Notably, if we calculate the SNR using only signals from the inner area, the actual SNR levels of Fig. 18(a) and (b) are estimated to be 4 and 14 dB, respectively, that is, their powers are -26 dB less than that of skin reflection. Figs. 19 and 20

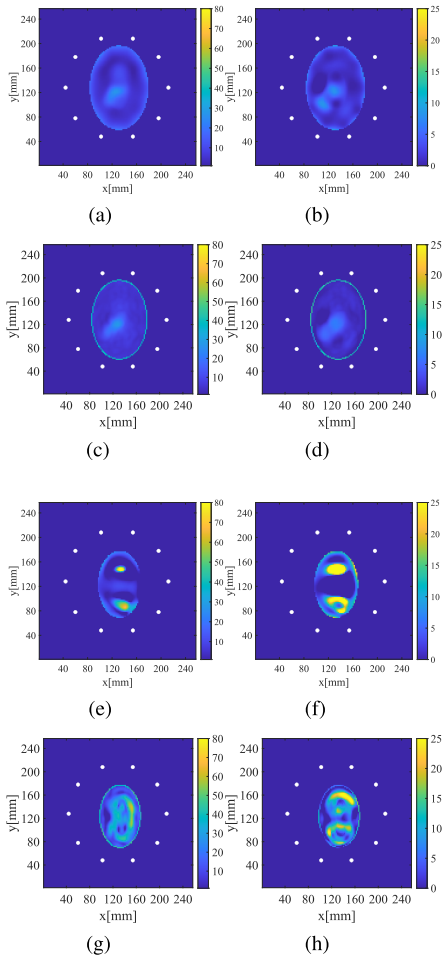

Fig. 17. Reconstruction results for CI and CSI images at 1.27 GHz in each method at the case for off-center located cancer. First column: $\Re[\epsilon]$. Second column: $\Im[\epsilon]$. (a) and (b) Original CSI, Class 1. (c) and (d) Proposed CSI, Class 1. (e) and (f) Original CSI, Class 4. (g) and (h) Proposed CSI, Class 4.

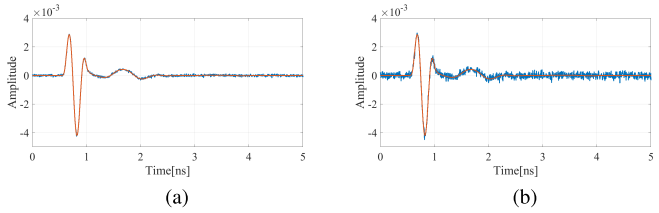

Fig. 18. Examples of reflection responses at each SNR level. Blue denotes the response with additive noise. Red and yellow denote the responses without and with skin reflection elimination, respectively, in the case of the absence of noise. (a) SNR = 40 dB. (b) SNR = 30 dB.

show the qualitative radar images by the CSI enhanced CI and its deconvolution image and illustrates the quantitative tomography images by the original and the proposed CSI methods, at the SNR levels of 30 and 40 dB, respectively. Table IX summarizes the RMSEs and ρ for each reconstructed real and imaginary parts of complex permittivity. As shown in these results, although the reconstruction results would suffer from inaccuracy for both CI and CSI images especially at the SNR of 30 dB, especially for Class 1, they could provide a certain level of accuracy in the case of an SNR of 40 dB. This is because the CI or CSI images highly depend on the SNR for the inner area, which is less than 10 dB in an SNR of 30 dB.

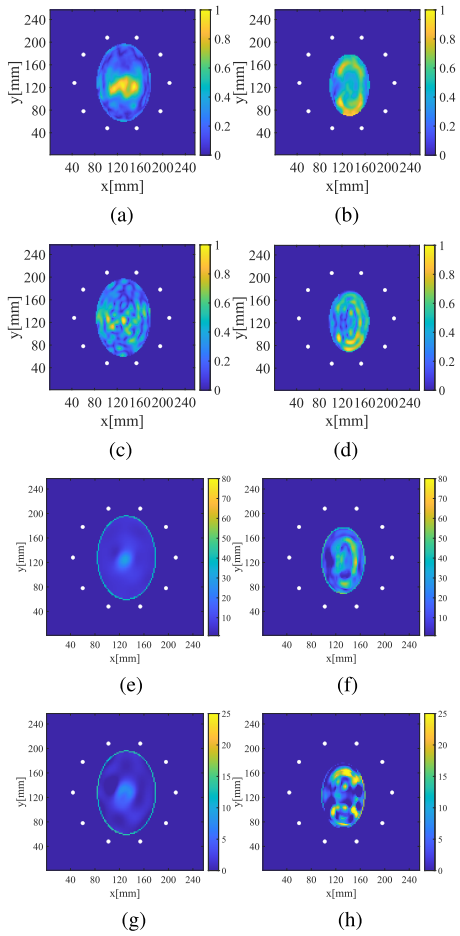

Fig. 19. Reconstruction results for CI and CSI images at 1.27 GHz in each method at the case in SNR of 40 dB. First column: Class 1. Second column: Class 4. (a) and (b) Cl. (c) and (d) Deconv. Cl. (e) and (f) Proposed CSI, $\Re(\epsilon)$. (g) and (h) Proposed CSI, $\Im(\epsilon)$.

TABLE IX
RMSE AND ρ IN EACH SNR LEVEL

	Class	RMSE		ρ	
		$\Re[\epsilon]$	$\Im[\epsilon]$	$\Re[\epsilon]$	$\Im[\epsilon]$
SNR = ∞ dB	Class 1	5.79	2.53	0.833	0.681
	Class 4	18.34	10.22	0.409	-0.091
SNR = 40 dB	Class 1	5.08	1.73	0.873	0.855
	Class 4	15.05	9.06	0.648	0.052
SNR = 30 dB	Class 1	22.67	6.70	0.301	0.023
	Class 4	15.94	10.17	0.612	-0.008

Furthermore, Figs. 21 and 22 also show the box plots of the RMSE for the real and imaginary parts of complex permittivity in Classes 1 and 4, respectively, where ten different patterns of additive noises are investigated to provide a statistically convincing conclusion. As shown in these analyses, there are nonnegligible variances of RMSEs, especially in the case with 30-dB SNR (4-dB SNR in considering only inner area signal), this is because the randomness of the noise component affects the optimal β to generate an initial estimate. By assuming a realistic scenario, it is promising to retain a sufficient SNR (over 10 dB) for the inner area by using the matching media, such as oil, to penetrate the inner area of the breast by suppressing the skin reflection signal.

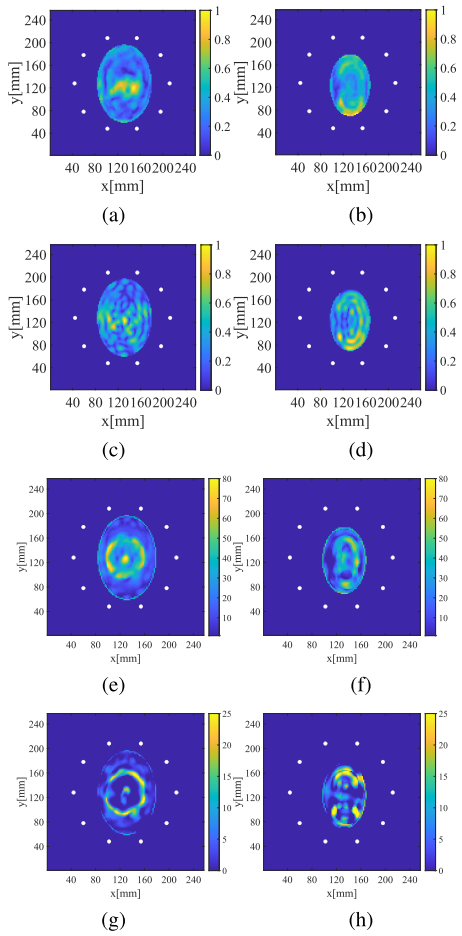

Fig. 20. Reconstruction results for CI and CSI images at 1.27 GHz in each method at the case in SNR of 30 dB. First column: Class 1. Second column: Class 4. (a) and (b) CI. (c) and (d) Deconv. CI. (e) and (f) Proposed CSI, $\Re(\epsilon)$. (g) and (h) Proposed CSI, $\Im(\epsilon)$.

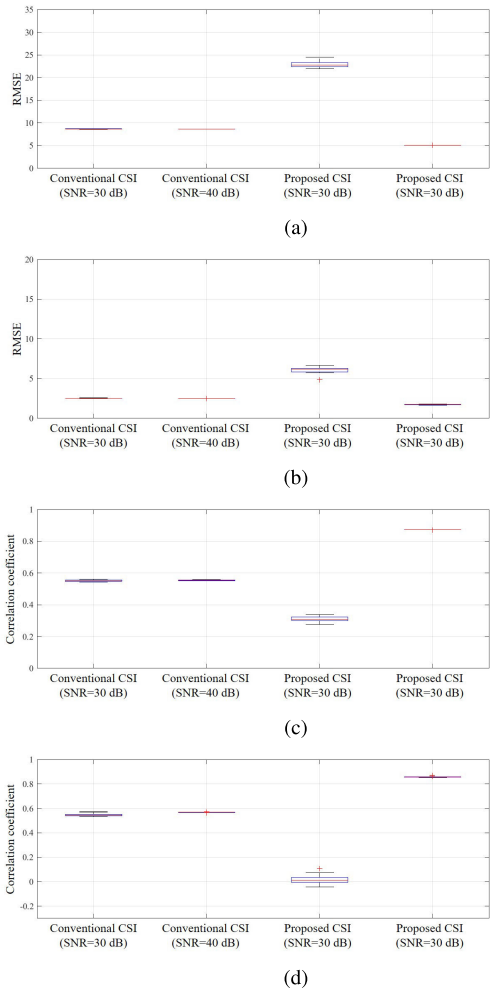

Fig. 21. Boxplots in each SNR level and method at Class 1. (a) RMSE for the real part. (b) RMSE for the imaginary part. (c) ρ for the real part. (d) ρ for the imaginary part.

E. Case for Multiple Frequency (MF) Extension

In the previous evaluation for the CSI-based reconstruction, we assume only a single frequency (SF) at 1.27 GHz. A number of studies revealed that MF inversion is promising for enhancing the reconstruction accuracy, especially in noisy situations, by alleviating the ill-posed conditions or averaging effects over frequencies. Here, we introduce the simple integration scheme for multiple-frequency results. At first, we obtain several complex permittivity results for each frequency. Then, these results are converted to the Debye parameter by minimizing the residual for the mean square errors, that is, the Debye fitting is applied. In this case, the two representative model Classes 1 and 4 are introduced in the absence of noise. Figs. 23 and 24 show the real and imaginary parts of the complex permittivity at each frequency in Class 1, respectively, obtained by the SF and MF inversion schemes. Figs. 25 and 26 also show the same views and conditions as those in Figs. 23 and 24, but for Class 4. Table X also shows the quantitative error analysis for this case. These results demonstrated that our proposed scheme using multifrequency data considerably enhances the reconstruction results in both real and imaginary parts of complex permittivity. This is because the variance of several SF results can be suppressed by the smoothing effect over MF results.

TABLE X

RMSE AND ρ FOR SF AND MF INVERSION SCHEMES IN THE PROPOSED METHOD AT CONDITION II

Class			RMSE		ρ	
			$\Re[\epsilon]$	$\Im[\epsilon]$	$\Re[\epsilon]$	$\Im[\epsilon]$
Class 1	1.27 GHz	SF	5.18	1.72	0.87	0.88
		MF	5.11	1.95	0.88	0.85
	2.19 GHz	SF	4.75	2.02	0.89	0.88
		MF	5.14	1.91	0.88	0.87
	3.11 GHz	SF	5.91	2.50	0.81	0.63
		MF	5.19	2.02	0.88	0.88
Class 4	1.27 GHz	SF	15.30	8.03	0.64	0.23
		MF	16.84	8.63	0.58	0.06
	2.19 GHz	SF	16.52	8.50	0.43	-0.08
		MF	16.93	6.52	0.59	0.19
	3.11 GHz	SF	20.59	6.07	0.41	0.19
		MF	17.08	5.96	0.59	0.32

F. Computational Complexity Comparison

Here, we investigate the computational complexity of each method. Table XI shows the complexity and the actual run time for each process, using an Intel Xeon Silver 4110 CPU 2.10 GHz with 384 GB RAM. Here, N_{ele}, N_{FR}, and N_{ROI}

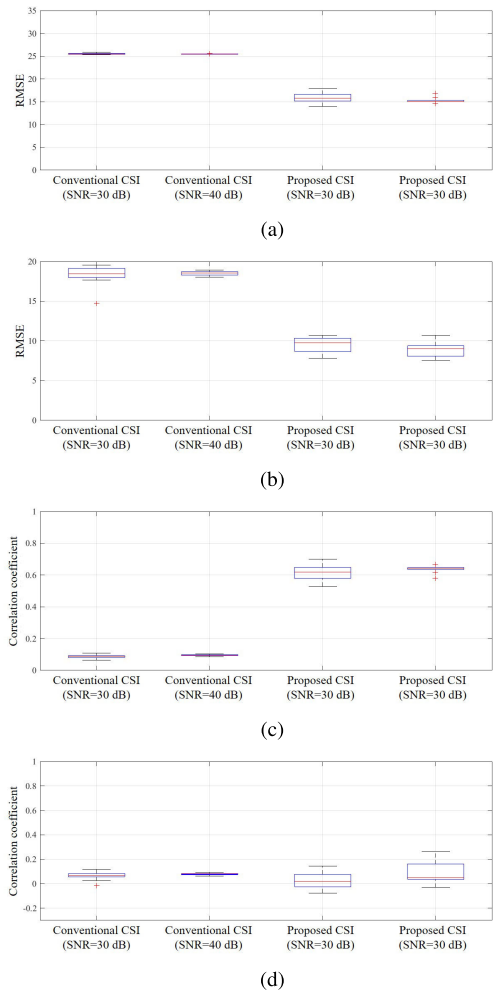

Fig. 22. Boxplots in each SNR level and method at Class 4. (a) RMSE for the real part. (b) RMSE for the imaginary part. (c) ρ for the real part. (d) ρ for the imaginary part.

TABLE XI

COMPUTATIONAL COMPLEXITY AND ACTUAL RUN TIME IN EACH PROCESS

Method	Step	Complexity	Run time
Original CSI		$O(N_{\rm ele}N_{\rm ROI}N_{\rm ite})$	800 s
Proposed method	1,2	$O(N_{\rm ele}N_{\rm ROI}N_{\rm FR}N_{\rm ite})$	9200 s
	3,4,5	$O(N_{\rm ele}N_{\rm ROI}N_{\rm FR})$	1500 s
	6	$O(N_{\rm ele}N_{\rm ROI}N_{\rm ite}N_{\beta})$	8000 s
	7	$O(N_{\rm ele}N_{\rm ROI}N_{\rm ite})$	800 s

express the numbers of elements, frequency samples, and cells in the ROI, respectively, which are the same for generating the CI and CSI images. $N_{\rm ite}$ denotes the number of iterations required in the CSI. N_β denotes the sampling number to determine β in (15) in Section III-B. Here, in both the original and proposed methods, $N_{\rm ele} = 100$, $N_{\rm FR} = 58$, $N_{\rm ROI} = 2594$, $N_\beta = 11$, and $N_{\rm ite} = 1000$, are set. As shown in this figure, the processes of Steps 2 and 6 require large computational times, because, in Step 2, the total fields in the ROI should be optimized at each frequency sample to obtain sufficient range resolution in the CI image, that is, an adequately wide frequency band is needed to determine the Green's function and clutter response. Meanwhile, in Step 6, the total fields in the ROI are also optimized at each β to determine an optimal

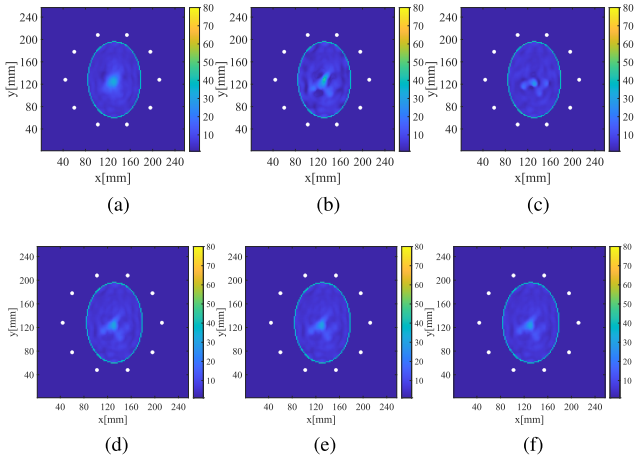

Fig. 23. Reconstruction results for the real part of complex permittivity with SF and MF inversion-based proposed method at each frequency at Class 1. (a) SF at 1.27 GHz. (b) SF at 2.19 GHz. (c) SF at 3.11 GHz. (d) MF at 1.27 GHz. (e) MF at 2.19 GHz. (f) MF at 3.11 GHz.

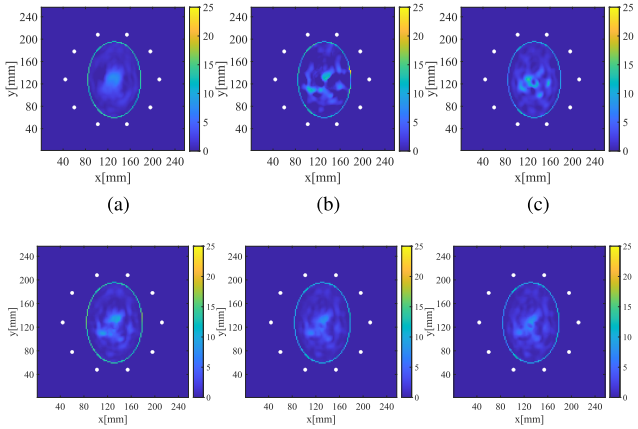

Fig. 24. Reconstruction results for the imaginary part of complex permittivity with SF and MF inversion-based proposed method at each frequency at Class 1. (a) SF at 1.27 GHz. (b) SF at 2.19 GHz. (c) SF at 3.11 GHz. (d) MF at 1.27 GHz. (e) MF at 2.19 GHz. (f) MF at 3.11 GHz.

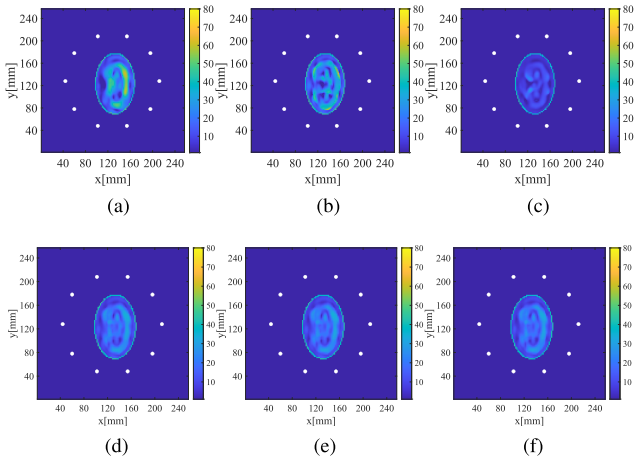

Fig. 25. Reconstruction results for the real part of complex permittivity with SF and MF inversion-based proposed method at each frequency at Class 4. (a) SF at 1.27 GHz. (b) SF at 2.19 GHz. (c) SF at 3.11 GHz. (d) MF at 1.27 GHz. (e) MF at 2.19 GHz. (f) MF at 3.11 GHz.

initial estimate. However, the complexity of this process could be significantly reduced by the undersampling scheme along the frequency domain. That is, if we obtain undersampled

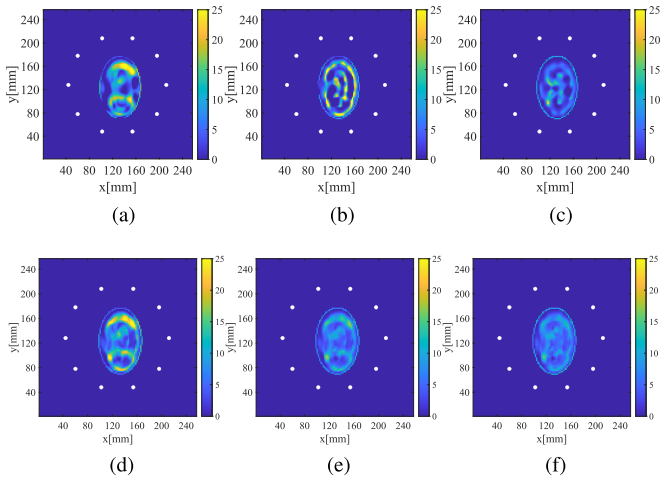

Fig. 26. Reconstruction results for the imaginary part of complex permittivity with SF and MF inversion-based proposed method at each frequency at Class 4. (a) SF at 1.27 GHz. (b) SF at 2.19 GHz. (c) SF at 3.11 GHz. (d) MF at 1.27 GHz. (e) MF at 2.19 GHz. (f) MF at 3.11 GHz.

data along the frequency band, these data can be accurately upsampled by using the Sinc function-based interpolation scheme because the sampling interval in the frequency domain (data length in the time domain) is generally sufficient to satisfy the above Nyquist criteria. The above reduction scheme should be implemented in our further study.

V. Conclusion

This article proposes a bidirectional processing scheme between radar and tomography for the quantitative microwave imaging of breast media. The traditional CI-based radar approach suffers from inaccuracy due to the heterogeneity of background media, which incurs an inaccuracy for posttomography-based quantitative reconstruction. Then, the CSI scheme was introduced as a tomography approach to enhance the radar-based CI image by providing an accurate form of the Green's function, assuming the heterogeneous skin-adipose media. This method also contributed a clutter suppression, particularly for the skin reflection signal, to generate these clutters using the DIE by exploiting the CSI outputs, namely the total fields in the ROI, thereby corresponding to the process of "tomography $\rightarrow$ radar." The numerical test validated that the CSI-based total field optimization could provide an accurate estimate of Green's function and clutter response at the same level as FDTD-based calculation. In addition, the proposed scheme introduced the CI image-enhanced CSI scheme to reproduce the quantitative reconstruction of the dielectric profile, formed as single-pole Debye parameters. The 2-D Gaussian function deconvolution scheme enhanced the equivalent spatial resolution of the CI image, which was exploited for an appropriate initial estimate for the post-CSI optimization sequences. This is the process called "radar $\rightarrow$ tomography."

Numerical tests using the MRI-derived realistic phantom and FDTD analysis demonstrated that the proposed bidirectional processing scheme successfully improved the reconstruction accuracy of the dielectric property, even for heterogeneous and high-contrast breast media. Notably, we did not introduce any lossy-matching (coupling) media to suppress the skin reflection response, which would be promising to enhance the SNR assuming realistic cases in further investigations. Furthermore, we should note the limitations of the 2-D simulation model for realistic scenarios. In this study, we assumed a 2-D TM mode propagation, which could be modeled as a linear polarization model, such as a dipole antenna, in the 3-D model. However, some works like [42] demonstrated that the scattered field includes not only copolarized (E_z), but also cross-polarized (E_x or E_z) components, especially for highly heterogeneous media. Thus, we need all three components of the electric total fields in the ROI, and the ill-posed condition would be extremely severe because of the considerably larger number of unknown cells. Our ongoing studies include 3-D model extensions, where the undersampling or Fourier basis scheme would be introduced to drastically decrease the number of unknowns, and the experimental, or clinical investigations are included in our future scope.

References

[1] M. Okayama, T. Nagaoka, and K. Sugisaki, "Cancer screening rate and related factors in the Japanese child-rearing generation," *Healthcare*, vol. 10, no. 3, p. 508, Mar. 2022.

[2] B. M. Moloney et al., "Microwave imaging in breast cancer–results from the First-In-Human clinical investigation of the Wavelia system," *Academic Radiol.*, vol. 29, no. 1, pp. 211–222, 2022.

[3] S. Kwon and S. Lee, "Recent advances in microwave imaging for breast cancer detection," *Int. J. Biomed. Imag.*, vol. 2016, pp. 1–26, Dec. 2016.

[4] M. Lazebnik et al., "A large-scale study of the ultrawideband microwave dielectric properties of normal, benign and malignant breast tissues obtained from cancer surgeries," *Phys. Med. Biol.*, vol. 52, pp. 2637–2656, Oct. 2007.

[5] Y. Cheng and M. Fu, "Dielectric properties for non-invasive detection of normal, benign, and malignant breast tissues using microwave theories," *Thoracic Cancer*, vol. 9, no. 4, pp. 459–465, Apr. 2018.

[6] T. M. Grzegorczyk, P. M. Meaney, P. A. Kaufman, R. M. di Florio-Alexander, and K. D. Paulsen, "Fast 3-D tomographic microwave imaging for breast cancer detection," *IEEE Trans. Med. Imag.*, vol. 31, no. 8, pp. 1584–1592, Aug. 2012.

[7] A. Modiri, S. Goudreau, A. Rahimi, and K. Kiasaleh, "Review of breast screening: Toward clinical realization of microwave imaging," *Med. Phys.*, vol. 44, no. 12, pp. e446–e458, Dec. 2017.

[8] E. C. Fear, X. Li, S. C. Hagness, and M. A. Stuchly, "Confocal microwave imaging for breast cancer detection: Localization of tumors in three dimensions," *IEEE Trans. Biomed. Eng.*, vol. 49, no. 8, pp. 812–822, Aug. 2002.

[9] H. Song et al., "Detectability of breast tumors in excised breast tissues of total mastectomy by IR-UWB-radar-based breast cancer detector," *IEEE Trans. Biomed. Eng.*, vol. 66, no. 8, pp. 2296–2305, Aug. 2019.

[10] A. Naghibi and A. R. Attari, "Near-field radar-based microwave imaging for breast cancer detection: A study on resolution and image quality," *IEEE Trans. Antennas Propag.*, vol. 69, no. 3, pp. 1670–1680, Mar. 2021.

[11] L. Guo and A. M. Abbosh, "Optimization-based confocal microwave imaging in medical applications," *IEEE Trans. Antennas Propag.*, vol. 63, no. 8, pp. 3531–3539, Aug. 2015.

[12] M. O'Halloran, M. Glavin, and E. Jones, "Improved confocal microwave imaging of the breast using path-dependent signal weighting," in *Proc. 30th URSI Gen. Assem. Sci. Symp.*, Aug. 2011, pp. 1–4.

[13] G. Umezu, Y. Yamauchi, and S. Kidera, "Contrast source inversion enhanced confocal imaging for highly heterogeneous breast media in microwave mammography," *IEEE J. Electromagn., RF Microw. Med. Biol.*, vol. 6, no. 4, pp. 494–500, Dec. 2022.

[14] P. M. van den Berg and A. Abubakar, "Contrast source inversion method: State of art," *Prog. Electromagn. Res.*, vol. 34, pp. 189–218, 2001.

[15] T. Rubaek, P. M. Meaney, P. Meincke, and K. D. Paulsen, "Nonlinear microwave imaging for breast-cancer screening using Gauss–Newton's method and the CGLS inversion algorithm," *IEEE Trans. Antennas Propag.*, vol. 55, no. 8, pp. 2320–2331, Aug. 2007.

[16] J. E. Johnson, T. Takenaka, and T. Tanaka, "Two-dimensional time-domain inverse scattering for quantitative analysis of breast composition," *IEEE Trans. Biomed. Eng.*, vol. 55, no. 8, pp. 1941–1945, Aug. 2008.

[17] M. T. Bevacqua, S. Di Meo, L. Crocco, T. Isernia, and M. Pasian, "Millimeter-waves breast cancer imaging via inverse scattering techniques," *IEEE J. Electromagn., RF Microw. Med. Biol.*, vol. 5, no. 3, pp. 246–253, Sep. 2021.

[18] F. Gao, B. D. Van Veen, and S. C. Hagness, "Sensitivity of the distorted born iterative method to the initial guess in microwave breast imaging," *IEEE Trans. Antennas Propag.*, vol. 63, no. 8, pp. 3540–3547, Aug. 2015.

[19] K. Noritake and S. Kidera, "Boundary extraction enhanced distorted born iterative method for microwave mammography," *IEEE Antennas Wireless Propag. Lett.*, vol. 18, no. 4, pp. 776–780, Apr. 2019.

[20] J. D. Shea, P. Kosmas, S. C. Hagness, and B. D. Van Veen, "Three-dimensional microwave imaging of realistic numerical breast phantoms via a multiple-frequency inverse scattering technique," *Med. Phys.*, vol. 37, no. 8, pp. 4210–4226, Aug. 2010.

[21] L. M. Neira, B. D. Van Veen, and S. C. Hagness, "High-resolution microwave breast imaging using a 3-D inverse scattering algorithm with a variable-strength spatial prior constraint," *IEEE Trans. Antennas Propag.*, vol. 65, no. 11, pp. 6002–6014, Nov. 2017.

[22] T. U. Gürbüz, B. Aslanyürek, A. Yapar, H. Sahintürk, and I. Akduman, "A nonlinear microwave breast cancer imaging approach through realistic body–breast modeling," *IEEE Trans. Antennas Propag.*, vol. 62, no. 5, pp. 2596–2605, May 2014.

[23] N. Abdollahi, I. Jeffrey, and J. LoVetri, "Improved tumor detection via quantitative microwave breast imaging using eigenfunction-based prior," *IEEE Trans. Comput. Imag.*, vol. 6, pp. 1194–1202, 2020.

[24] H. Sato and S. Kidera, "ROI limited unknowns reduction-based contrast source inversion for microwave breast imaging," *IEEE Antennas Wireless Propag. Lett.*, vol. 19, no. 12, pp. 2285–2289, Dec. 2020.

[25] H. Sato and S. Kidera, "Noise-robust microwave breast imaging applied to multi-frequency contrast source inversion," *IEEE J. Electromagn., RF Microw. Med. Biol.*, vol. 5, no. 2, pp. 187–193, Jun. 2021.

[26] U. Yildirim, I. Dilman, E. Bilgin, S. Dogu, M. Çayören, and I. Akduman, "Continuous monitoring of hemorrhagic brain strokes via contrast source inversion," in *Proc. 11th Eur. Conf. Antennas Propag. (EUCAP)*, Mar. 2017, pp. 408–411.

[27] V. Mariano, J. A. T. Vasquez, and F. Vipiana, "A novel discretization procedure in the CSI-FEM algorithm for brain stroke microwave imaging," *Sensors*, vol. 23, no. 1, p. 11, Dec. 2022.

[28] M. J. Burfeindt, J. D. Shea, B. D. Van Veen, and S. C. Hagness, "Beamforming-enhanced inverse scattering for microwave breast imaging," *IEEE Trans. Antennas Propag.*, vol. 62, no. 10, pp. 5126–5132, Oct. 2014.

[29] A. Baran, D. J. Kurrant, A. Zakaria, E. C. Fear, and J. LoVetri, "Breast imaging using microwave tomography with radar-based tissue-regions estimation," *Prog. Electromagn. Res.*, vol. 149, pp. 161–171, 2014.

[30] O. Fiser et al., "UWB bowtie antenna for medical microwave imaging applications," *IEEE Trans. Antennas Propag.*, vol. 70, no. 7, pp. 5357–5372, Jul. 2022.

[31] D. Kurrant and E. Fear, "Regional estimation of the dielectric properties of inhomogeneous objects using near-field reflection data," *Inverse Problems*, vol. 28, no. 7, Jul. 2012, Art. no. 075001.

[32] N. Abdollahi, D. Kurrant, P. Mojabi, M. Omer, E. Fear, and J. LoVetri, "Incorporation of ultrasonic prior information for improving quantitative microwave imaging of breast," *IEEE J. Multiscale Multiphys. Comput. Techn.*, vol. 4, pp. 98–110, 2019.

[33] N. Irishina et al., "Structural level set inversion for microwave breast screening," *Inverse Probl.*, vol. 26, Feb. 2010, Art. no. 035015.

[34] T. J. Colgan, S. C. Hagness, and B. D. Van Veen, "A 3-D level set method for microwave breast imaging," *IEEE Trans. Biomed. Eng.*, vol. 62, no. 10, pp. 2526–2534, Oct. 2015.

[35] G. G. N. Geweid and M. A. Abdallah, "A novel approach for breast cancer investigation and recognition using M-level set-based optimization functions," *IEEE Access*, vol. 7, pp. 136343–136357, 2019.

[36] K. Noritake and S. Kidera, "Surface clutter suppression with FDTD recovery signal for microwave UWB mammography," *IEICE Trans. Electron.*, vol. E103.C, no. 1, pp. 26–29, Jan. 2020.

[37] W. Zhi and F. Chin, "Entropy-based time window for artifact removal in UWB imaging of breast cancer detection," *IEEE Signal Process. Lett.*, vol. 13, no. 10, pp. 585–588, Oct. 2006.

[38] H. Song et al., "A two-stage rotational surface clutter suppression method for microwave breast imaging with multistatic impulse-radar detector," *IEEE Trans. Instrum. Meas.*, vol. 69, no. 12, pp. 9586–9598, Dec. 2020.

[39] UWCEM. *Numerical Breast Phantom Repository*. [Online]. Available: https://uwcem.ece.wisc.edu/phantomRepository.html

[40] E. Zastrow, S. K. Davis, M. Lazebnik, F. Kelcz, B. D. Van Veen, and S. C. Hagness, "Development of anatomically realistic numerical breast phantoms with accurate dielectric properties for modeling microwave interactions with the human breast," *IEEE Trans. Biomed. Eng.*, vol. 55, no. 12, pp. 2792–2800, Dec. 2008.

[41] C. E. Chávez et al., "Avoiding the inverse crime in the inverse problem of electrocardiography: Estimating the shape and location of cardiac ischemia," in *Proc. Comput. Cardiol.*, Sep. 2013, pp. 687–690.

[42] P. Zhu, H. Morimoto, and S. Kidera, "Polarimetry effect in three-dimensional contrast source inversion for microwave breast imaging," in *Proc. IEEE USNC-URSI Radio Sci. Meeting (Joint With AP-S Symp.)*, Dec. 2021, pp. 76–77.

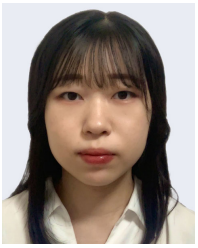

Mutsuki Nakajima received the B.E. degree in communication engineering and informatics from The University of Electro-Communications, Tokyo, Japan, in 2023, where she is currently pursuing the M.E. degree with the Graduate School of Informatics and Engineering.

Her research interests include inverse scattering and radar signal processing for microwave biomedical applications.

Shouhei Kidera (Senior Member, IEEE) received the B.E. degree in electrical and electronic engineering and the M.I. and Ph.D. degrees in informatics from Kyoto University, Kyoto, Japan, in 2003, 2005, and 2007, respectively.

In 2009, he joined The University of Electro-Communications, Tokyo, Japan, as an Assistant Professor, where he is currently a Full Professor with the Graduate School of Informatics and Engineering. He stayed at the Cross-Disciplinary Electromagnetics Laboratory, University of Wisconsin–Madison, Madison, WI, USA, as a Visiting Researcher, in 2016. He was a Principal Investigator of the PRESTO Program, Japan Science and Technology Agency (JST), from 2017 to 2021. His current research interests include advanced radar signal processing or electromagnetic inverse scattering issues for ultra-wideband (UWB) 3-D sensors or biomedical applications.

Dr. Kidera is a Senior Member of the Institute of Electronics, Information and Communication Engineers (IEICE), Japan, and the International Union of Radio Science (Union Radio-Scientifique Internationale, URSI); and a member of the Institute of Electrical Engineering of Japan (IEEJ) and the Japan Society of Applied Physics (JSAP). He was a recipient of the 2012 Ando Incentive Prize for the Study of Electronics, the 2013 Young Scientist's Prize by the Japanese Ministry of Education, Culture, Sports, Science and Technology (MEXT), the 2014 Funai Achievement Award, the 2022 KDDI Foundation Award, the Contribution Award, and the 2023 Research Institute of Electrical Communication (RIEC) Award.